

Gravitational Waves from Confinement in $SU(N)$ Yang-Mills Theory

Stephan Huber ^{*}, Rory Phipps [†] and Manuel Reichert [‡]

Department of Physics and Astronomy, University of Sussex, Brighton, BN1 9QH, U.K.

We provide a detailed analysis of the gravitational wave spectrum of $SU(N)$ pure Yang-Mills theory. The confinement phase transition is described with an effective Polyakov loop model, using the latest lattice data as an input. In particular, recent lattice studies clarified the large- N scaling of the surface tension, which we incorporate through a modification of the kinetic term. We demonstrate that the thin-wall approximation agrees with the Polyakov loop model at small N while it breaks down at large N . Furthermore, we include reliable estimates of the bubble wall velocity using a recently developed framework based on a large enthalpy jump at the phase transition. Altogether, this allows us to derive the gravitational wave signals for all $SU(N)$ confinement phase transitions and clarifies the behaviour at large N . The strongest signal arises for $N = 20$, but overall the predicted signals remain rather weak. Our work paves the way for future studies of other gauge groups and systems with fermions.

I. INTRODUCTION

QCD-like dark sectors are interesting and well-motivated extensions of the Standard Model. Being asymptotically free at high energies, they are naturally UV-complete and, in the IR, predict fascinating bound-state dark matter candidates such as dark baryons, dark mesons, or even dark glueballs [1–8]. While the QCD transition is a crossover, various strongly-coupled theories exhibit a first-order confinement phase transition. The stochastic background of gravitational waves (GWs) generated by such a phase transition can be used to constrain the corresponding dark sector. It is therefore of great importance to be able to accurately compute this signal in preparation for planned and future experiments.

The study of first-order phase transitions (FOPTs) in a strongly-interacting theory is, in general, a challenging task. Due to the strong dynamics, one cannot rely on perturbation theory and instead must turn to non-perturbative methods. Non-perturbative methods can provide access to quantities of interest for the computation of the GW power spectrum. These are typically equilibrium quantities, such as the latent heat, interface tension, and pressure computed on the lattice [9–16], or an effective potential from functional methods [17–22] or holography [23–32]. Non-equilibrium quantities necessary for the computation of the GW spectrum, such as the bubble nucleation rate and the wall velocity, are less easily accessible using these techniques. Often, such non-perturbative methods will therefore be used in tandem with an effective description of the phase transition [33–43].

In this work, we study pure Yang-Mills dark sectors. These are the simplest choice of a strongly coupled dark sector, and allow us to make use of the abundance of non-perturbative results, in particular lattice data. Furthermore, the order parameter for the confinement phase

transition is well understood. These sectors provide dark glueballs as a dark matter candidate; however, in practice, most of the parameter space is ruled out if one insists on single-component dark matter [5, 6]. The only viable regime is that where the dark sector is much colder than the visible sector, but in this scenario it would constitute a very small fraction of the energy density of the Universe, resulting in a weak GW signal. Despite not being a realistic dark matter candidate, our work aims to provide a detailed understanding of the phase transition of a QCD-like hidden sector, which can be extended to more realistic dark sectors in the future. We analyse the confinement phase transition of a pure $SU(N)$ theory. This phase transition is of first order for $N \geq 3$, and the expectation value of the Polyakov loop is the order parameter. As such, the effective Polyakov loop model (PLM) [44, 45] is well suited to describe the thermodynamics of the phase transition. Here, we build on previous works [38] where an effective tunnelling action was constructed, and the coefficients of the effective Polyakov loop potential were fitted to lattice data [12, 13].

Recent lattice results [14] demonstrated that the interface tension of the phase transition scales as $\sigma \propto N^2$ at large N , which is incompatible with the PLM formulated in [38]. To reconcile this, we extend the setup by modifying the kinetic term in the effective Polyakov loop action, such that the model matches the results of the interface tension exactly. This leads us to a more accurate reconstruction of the Polyakov loop action, suitable for the study of bubble nucleation in the FOPT.

To determine the GW power spectrum, we use the results of numerical simulations [46–51], which express the spectrum in terms of a set of parameters, namely the nucleation temperature, duration, strength parameter, and wall velocity. While the former three quantities can be computed directly from the effective Polyakov loop action, the latter requires non-equilibrium information. In this work, we employ novel developments in the computation of the bubble wall velocity [52] valid when there is a large change in the number of degrees of freedom at the transition. The error on these parameters is estimated directly from the uncertainty in the lattice results used

^{*} s.huber@sussex.ac.uk

[†] r.phipps@sussex.ac.uk

[‡] m.reichert@sussex.ac.uk

in the fitting procedure.

The results from the effective Polyakov loop model are compared to those from the thin-wall approximation, which relies only on the interface tension and latent heat computed on the lattice. We demonstrate at small N that the thin-wall approximation is well suited to determine the nucleation temperature and the duration of the phase transition. This agreement is stronger than in previous computations since our PLM matches the surface tension exactly due to the generalised kinetic term. At large N , the thin-wall approximation predicts a large degree of supercooling, which is a prediction outside of its domain of validity. We indeed confirm the breakdown of this approximation at large N , as the Polyakov loop model predicts a maximum degree of supercooling. This is due to the disappearance of the barrier in the effective potential that separates the true and false vacuum, and occurs close to the critical temperature.

With the PLM, we are able to determine the GW power spectrum at large N . We show that the peak amplitude has a maximum for $N = 20$ and rapidly decays as $h^2\Omega_{\text{GW}}^{\text{peak}} \propto N^{-14/3}$ at large N . Overall, the signals are weak and, unfortunately, undetectable at planned and future GW observatories. This is a result of the strong coupling of the dark sector, which leads to a rapidly changing effective potential below the critical temperature. As a consequence, these transitions have a very short duration, which suppresses the signal. Given the consistency of our framework with lattice results, it can now be extended to study Yang-Mills theories of different gauge groups, or perhaps theories containing fermions in different representations, which provide more compelling dark matter candidates.

This paper is structured as follows: in [Sec. II](#) we introduce the thin-wall approximation as the simplest method with which one can estimate the GW signal. It relies only on input from the latent heat and interface tension, both of which have been computed on the lattice, but we demonstrate that its validity is restricted to small gauge groups. We improve upon the thin-wall approximation with the PLM in [Sec. III](#). Here, we extend previous computations by modifying the model such that the PLM can reproduce new results of the interface tension at large N . In [Sec. IV](#) we present the results of our computations of the GW parameters, including error estimates and their large- N scaling. These enter into the final computation of the GW power spectrum, the results of which we display in [Sec. V](#) alongside the signal-to-noise ratios at planned and future detectors. We summarise and conclude in [Sec. VI](#).

II. THIN-WALL APPROXIMATION

The thin-wall approximation is a common approach to obtain the relevant thermodynamic quantities for the GW spectrum from first-order cosmological phase transitions. The appeal of this approach lies in its mathematical

simplicity; under the assumption of thin-walled bubbles, an analytic expression for the Euclidean action can be derived [\[53\]](#). In our case, this greatly simplifies the analysis of the $SU(N)$ confinement transition, where relevant quantities such as the interface tension, σ , and latent heat, L , have been computed on the lattice [\[12, 14\]](#).

The thin-wall approximation is an expansion in $(T - T_c)/T_c$, where T_c is the critical temperature, at which the two phases are degenerate in free energy. Naturally, the expectation is that the thin-wall approximation works well when the nucleation temperature, T_n , is close to T_c . However, whether or not the thin-wall approximation truly holds for the system of interest must be verified by a computation from the full effective potential; in our case, the effective potential of the Polyakov loop presented in [Sec. III](#). Indeed, a notable result of this work is that the thin-wall approximation is insufficient for extracting the thermodynamics of the first-order confinement transition in the large- N limit. Below, we outline the logic of the approximation, see also [\[38, 41, 54–57\]](#), and in [Sec. IV A](#) we demonstrate its breakdown.

The critical bubble is a non-trivial field configuration that interpolates between the true and false vacua of the system, satisfying the equation of motion and boundary conditions, as we will detail later in [Sec. III B](#). If a bubble is assumed to have a thin wall, such that the bubble radius is much larger than the wall thickness, the three-dimensional Euclidean action can be approximated by

$$S_3(T, R) = 4\pi\sigma R^2 - \frac{4\pi}{3}R^3\Delta p, \quad (1)$$

where Δp denotes the pressure difference between the confined and deconfined phases, and R is the bubble radius. In this regime, the action is assumed to be dominated by contributions from an infinitesimal bubble wall and the bulk volume, corresponding to the first and second terms of [\(1\)](#), respectively. The critical radius is given by

$$R_c = \frac{2\sigma}{\Delta p}, \quad (2)$$

which is obtained as the stationary point of the bubble action with respect to R . Substitution of this expression into [\(1\)](#) yields the thin-wall approximation for the energy of the critical bubble,

$$S_3(T) = \frac{16\pi}{3} \frac{\sigma^3}{\Delta p^2}. \quad (3)$$

Expanding the pressure difference, $\Delta p \equiv \Delta p(T)$, around T_c we find

$$\begin{aligned} \Delta p(T) &\simeq \Delta p(T_c) + (T - T_c) \left. \frac{d(\Delta p)}{dT} \right|_{T=T_c} \\ &= (T - T_c) \left. \frac{d(\Delta p)}{dT} \right|_{T=T_c} \equiv L \frac{(T - T_c)}{T_c}, \end{aligned} \quad (4)$$

where we have defined the latent heat of the transition, L . Truncation of the expansion up to first-order is valid if $T \simeq$

T_c . The Euclidean action in the thin-wall approximation then reduces to

$$S_3(T) = \frac{16\pi}{3} \frac{\sigma^3}{L^2} \frac{T_c^2}{(T - T_c)^2}. \quad (5)$$

The result in (5) is valid for any theory. For $SU(N)$ Yang-Mills theory, (5) is particularly useful since it is written entirely in terms of quantities that have been computed on the lattice for small N and have associated large- N fits [12, 14]. Interestingly, the lattice work [14] has demonstrated that the interface tension scales as N^2 in the large N limit, clarifying the uncertainty of the large- N scaling observed in [12]. When investigating the thin-wall approximation at large N we employ the large- N formulae of the interface tension and latent heat from [14],

$$\begin{aligned} \frac{\sigma}{T_c^3} &= 0.0182(7)N^2 - 0.194(15), & N \geq 4, \\ \frac{L}{T_c^4} &= 0.360(6)N^2 - 1.88(17), & N \geq 5. \end{aligned} \quad (6)$$

Substitution of these expressions into (5) yields an expression for the action in the thin-wall approximation that scales as N^2 in the large- N limit,

$$S_3^{(N \geq 5)}(T) = \frac{16\pi}{3} \frac{(0.0182N^2 - 0.194)^3}{(0.360N^2 - 1.88)^2} \frac{T_c^3}{(T - T_c)^2}. \quad (7)$$

This is the expected scaling for a system that is dominated by $N^2 - 1$ degrees of freedom. It is important to note that the temperature-dependence of the action stems entirely from the $1/(T - T_c)^2$ term, which is the source of the thin-wall approximation's prediction for the degree of supercooling.

III. POLYAKOV LOOP MODEL

Following the work of 't Hooft, Svetitsky, and Yaffe [58–60], it has been established that the vacuum expectation value (VEV) of the Polyakov loop is an order parameter for the confinement phase transition in Yang-Mills theory at finite temperature. Pisarski subsequently pioneered the practical mean field theory approach to study confinement that forms the foundation of this work [44, 45].

The first part of this section briefly motivates the Polyakov loop as an order parameter for confinement through an examination of the relevant symmetries. We then discuss the effective theory of the Polyakov loop that was used in this study, highlighting the importance of results from lattice computations in refining the model. Given the recent developments made in calculating the interface tension on the lattice [14], this study builds on the work of [38] by modifying their Polyakov loop model to match these new results. The PLM predictions for the interface tension and latent heat are then displayed with a direct comparison to the large- N fits in [12] and

[14]. The exact agreement observed between the lattice results and the PLM in both of these two quantities, for the entire range of N , demonstrates the model's ability to compute the thermodynamics of the FOPT.

A. The Polyakov Loop

In Euclidean time, τ (not to be confused with $\tau = T/T_c$ in later sections), at finite temperature, the temporal direction of spacetime is compactified with period $\beta = 1/T$. The gauge fields are required to obey the periodic boundary conditions

$$A_\mu(\tau + \beta, \mathbf{x}) = A_\mu(\tau, \mathbf{x}). \quad (8)$$

Under local symmetry transformations, in our case belonging to the group $SU(N)$, the gauge fields must continue to satisfy (8). Given this assertion, it is easy to show that the allowed gauge transformations, applied using matrices $\Omega(\mathbf{x}, \tau) \in SU(N)$, must satisfy the less stringent condition that they are periodic in Euclidean time up to an element of the centre of the gauge group:

$$\Omega(\tau + \beta, \mathbf{x}) = z \Omega(\tau, \mathbf{x}), \quad z \in Z_N, \quad (9)$$

where Z_N is the centre of $SU(N)$. Specifically, the subset of gauge transformations that are not continuously connected to the identity, due to the nontrivial topology of the temporal direction, consists of transformations that are periodic up to an element of the centre. These form a group of global transformations, known as centre transformations, that are a symmetry of the action.

Operators that wrap around the thermal circle are sensitive to these global transformations. An example of such an operator is the Polyakov loop,

$$\ell(\mathbf{x}) = \frac{1}{N} \text{Tr} [\mathbf{L}(\mathbf{x})], \quad (10)$$

which is defined in terms of the thermal Wilson line,

$$\mathbf{L}(\mathbf{x}) = \mathcal{P} \exp \left[ig \int_0^\beta d\tau A_0(\tau, \mathbf{x}) \right], \quad (11)$$

where \mathcal{P} denotes path ordering, g is the gauge coupling, and $A_0(\tau, \mathbf{x})$ is the zeroth component of the gauge field. As the gauge field is matrix-valued, $A_\mu(\tau, \mathbf{x}) = A_\mu^a(\tau, \mathbf{x}) T^a$ with T^a the generators of $SU(N)$ and $a = 1, 2, \dots, N^2 - 1$, the thermal Wilson line transforms nontrivially under local symmetry transformations. Indeed, it is itself an $SU(N)$ matrix and can be shown to transform in the following way:

$$\begin{aligned} \mathbf{L}(\mathbf{x}) &\rightarrow \Omega^\dagger(\beta, \mathbf{x}) \mathbf{L}(\mathbf{x}) \Omega(0, \mathbf{x}) \\ &= z \Omega^\dagger(0, \mathbf{x}) \mathbf{L}(\mathbf{x}) \Omega(0, \mathbf{x}), \quad z \in Z_N. \end{aligned} \quad (12)$$

As the traced thermal Wilson line, the Polyakov loop is gauge invariant and can be thought of as a complex scalar

N	a_0	a_1	a_2	a_3	a_4	b_3	b_4	b_5	b_6	b_8
3	6.24	-5.78	8.67	-7.99	-1.93	-2.26	3.26	-	-	-
4	10.1	-8.85	10.0	-12.3	0.41	-	-1.84	-	2.91	-
5	15.2	-11.6	3.77	0.21	-9.68	-	-9.04	10.3	-	-
6	22.8	-29.4	66.9	-96.3	29.8	-	-19.9	-	36.9	-14.9

Table 1. Parameter values obtained from χ^2 -fitting of the Polyakov loop effective potential for $N = 3, 4, 5$, and 6, using the procedure described in [Sec. III B](#).

field that is charged under centre transformations. From (12) it transforms as

$$\ell(\mathbf{x}) \rightarrow z \ell(\mathbf{x}), \quad z \in Z_N. \quad (13)$$

We emphasise that local gauge transformations and global centre transformations act independently. Indeed, in (12) one can set $z = 1$ such that the transformation is purely local, and by the cyclic property of the trace, the Polyakov loop is clearly invariant under these local symmetry transformations. Conversely, a centre transformation in $SU(N)$ maps the system to one of its N degenerate ground states in the deconfined phase. Although these vacua are physically equivalent, the Polyakov loop is charged under these global transformations, and it measures the extent to which this symmetry is spontaneously broken/restored.

Through its definition in terms of the thermal Wilson line, the VEV of the Polyakov loop is interpreted to be related to the free energy of a static quark, E_q , via

$$\langle \ell \rangle = \exp\left(-\frac{E_q}{T}\right). \quad (14)$$

Since a static quark is a colour source, in the low-temperature confined phase it takes an infinite amount of energy to isolate, such that $\langle \ell \rangle = 0$. Conversely, in the high-temperature deconfined phase, quarks are allowed states with finite free energy, such that $\langle \ell \rangle \neq 0$. Considering a Polyakov loop effective theory, the overall picture is the following: at high temperatures, the Polyakov loop has a non-zero VEV and the global centre symmetry is spontaneously broken. Once the temperature drops below the critical temperature, the Polyakov loop VEV vanishes, and the centre symmetry is spontaneously restored. Thus, the VEV of the Polyakov loop acts as an order parameter for the confinement phase transition in pure Yang-Mills theory. Such an effective theory can, in principle, be derived directly from the action of the full theory. As discussed in [Sec. III B](#), an alternative approach is to write down a simple effective potential in terms of free parameters which preserves the Z_N symmetry, and fit the potential to lattice data [\[37–43, 61\]](#).

It should be noted that the introduction of dynamical quarks in the fundamental representation explicitly breaks centre symmetry, such that the Polyakov loop is no longer an exact order parameter. More precisely, a general centre transformation on fundamental quarks violates the antiperiodic boundary condition they must satisfy at finite

temperature. In this scenario, the transition remains of first order only if the quark masses are significantly larger than the confinement scale [\[61–63\]](#). This is important in QCD-like theories. In theories with dynamical quarks in certain higher representations, the Polyakov loop remains a strict order parameter [\[64\]](#).

B. Polyakov Loop Effective Action

In principle, it is possible to derive an effective action written in terms of the traced thermal Wilson line directly from the Yang-Mills action of the theory. To do this analytically, however, will inevitably require approximations. After the work of Svetitsky and Yaffe [\[60\]](#), many attempts at this were made [\[65–69\]](#). See [\[70\]](#) for a review on this subject.

To study the confinement transition at large N , it becomes clear that such analytic approaches will not suffice, and input from lattice results is required. One alternative approach is to write down an effective potential which preserves the Z_N symmetry in terms of a set of free parameters, and fix these parameters using results obtained from lattice computations. Indeed, this is the method employed in [\[38\]](#) upon which our work is based. The simplest potential one can write down that preserves the Z_N symmetry and exhibits a FOPT reads,

$$V_{\text{eff}}^N(\ell, T) = T^4 \left(A |\ell|^2 + B |\ell|^4 + C (\ell^N + \ell^{*N}) + \dots \right), \quad (15)$$

where the factor of T^4 ensures the correct dimensionality of the potential. While the dimensionless coefficients A , B , and C are generally temperature-dependent, in [\[61, 70\]](#) it is reasoned that only the coefficient A needs to be temperature-dependent to capture the necessary effects.

The VEV of the Polyakov loop is, in general, a complex number; however, the Z_N symmetry of the potential allows one to choose a convenient direction. Denoting by ℓ_0 the magnitude of the VEV of the Polyakov loop, which is temperature-dependent, it is easy to see that

$$\langle \ell \rangle = \ell_0 \exp\left(i \frac{2\pi j}{N}\right), \quad j = 0, 1, \dots, N-1, \quad (16)$$

for temperatures above the critical. We choose $j = 0$, which simplifies the form of the potential in (15) as ℓ is

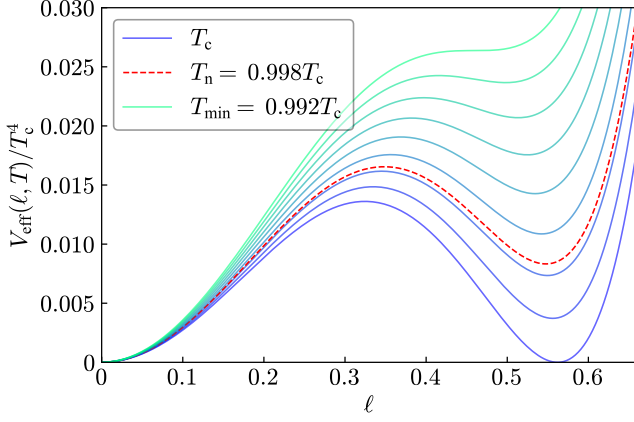


Figure 1. Reconstructed $SU(4)$ Polyakov loop effective potential, in units of T_c^4 , plotted as a function of the Polyakov loop along the real direction. Each curve was obtained for a given temperature, ranging from the critical temperature, T_c , to T_{\min} ; the temperature at which the barrier disappears.

strictly real, such that $\ell = \ell^*$. Therefore, the following ansatz for the Polyakov loop effective potential was used

$$V_{\text{eff}}^N(\ell, T) = T^4 \left(-\frac{b_2(T)}{2} \ell^2 + \sum_{i=3}^{i_{\max}} b_i \ell^i \right), \quad (17)$$

where we have rewritten the polynomial coefficients of (15) in terms of parameters b_j , and

$$b_2(T) = a_0 + a_1 \left(\frac{T_c}{T} \right) + a_2 \left(\frac{T_c}{T} \right)^2 + a_3 \left(\frac{T_c}{T} \right)^3 + a_4 \left(\frac{T_c}{T} \right)^4. \quad (18)$$

For our purposes, truncating the sum at $i_{\max} = 8$ was sufficient. Note that for a given value of N , not all terms in the effective potential in (17) contribute. Firstly, the required Z_N symmetry forces certain terms to be exactly zero; for instance, $b_3 = b_5 = b_7 = 0$ in the $SU(6)$ potential. Additionally, in certain small- N cases, higher-order terms were found to be irrelevant and so were dropped for simplicity. This is shown in Tab. 1.

In [38], each free parameter was obtained by fitting the potential in (17) to lattice results of the pressure and the trace of the energy-momentum tensor as a function of temperature [13] for $N = 3, 4, 5, 6$, and 8. The χ^2 -minimisation was subject to the constraint $\langle \ell \rangle \rightarrow 1$ when $T \rightarrow \infty$, as well the Stefan-Boltzmann limit, $p/T^4|_{T \rightarrow \infty} \rightarrow 1.21 \cdot (N^2 - 1) \cdot \pi^2/45$ [13].

Here, we improve the fitting procedure in two ways. Firstly, we include the latest latent heat results from the lattice in the fitting procedure. We employ the infinite-volume-extrapolated values of the latent heat from [71] and [14] for $N = 3$ and $N = 4, 5, 8$, respectively, whereas for $N = 6$ the large- N formula in (6) was used. As an example, we show the $N = 4$ Polyakov loop effective potential obtained using this fitting method in Fig. 1. To ascertain the significance of the introduction of the latent heat into the fitting procedure, one can compare the

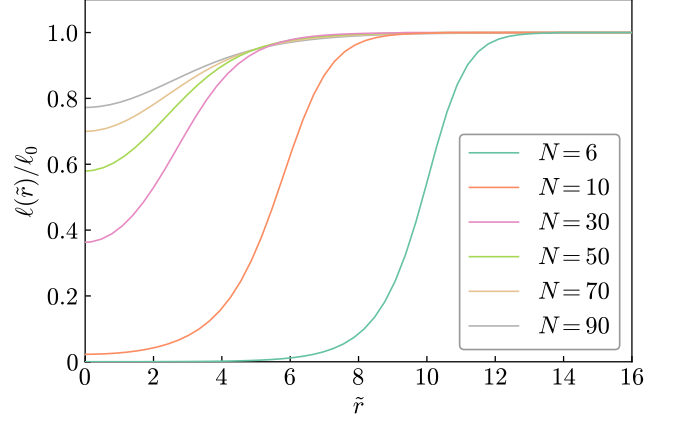


Figure 2. Bounce solution obtained at the nucleation temperature, scaled by the Polyakov loop VEV, $\ell_0(T = T_n)$, and plotted as a function of the dimensionless radius, $\tilde{r} = rT_c$, for various values of N . A critical temperature of $T_c = 1$ GeV was used.

parameter values displayed in Tab. 1 to those obtained in the work of [38] (noting the different conventions in defining the coefficients). The largest change in the parameter values occurred for the $SU(3)$ effective potential, which can be attributed to the significantly different value for the latent heat obtained in the recent study of [71] as compared to that predicted by the data in [13]. The incompatibility of these data is a source of uncertainty discussed in Sec. V C. The parameters of the $N = 4, 5$ and 6 effective potentials changed only slightly.

Secondly, we improve the treatment of the kinetic term in the Polyakov loop effective action. In [38, 39], a canonical kinetic term for the thermal Wilson line was assumed; however, as we will show, this results in a prediction for the interface tension which does not match the N^2 scaling displayed in (6). Remaining ignorant about the form of the kinetic term and imposing spherical symmetry, the Polyakov loop three-dimensional Euclidean action reads

$$S_3(T) = 4\pi T \int_0^\infty dr' r'^2 \left[\frac{Z_\ell}{2} \left(\frac{d\ell}{dr'} \right)^2 + V'_{\text{eff}}(\ell, T) \right], \quad (19)$$

where $r' = rT$, with r the radial coordinate, $V'_{\text{eff}}(\ell, T) = V_{\text{eff}}/T^4$, and Z_ℓ is in general some undetermined function of the Polyakov loop and the temperature, which is taken to be field- and temperature-independent here. For a canonical kinetic term, $Z_\ell = 1$. To obtain the bubble profile, we solve the Euler-Lagrange equation of motion,

$$\frac{d^2 \ell}{dr'^2} + \frac{2}{r'} \frac{d\ell}{dr'} - \frac{1}{Z_\ell} \frac{\partial V'_{\text{eff}}(\ell, T)}{\partial \ell} = 0, \quad (20)$$

subject to the boundary conditions

$$\left. \frac{d\ell}{dr'} \right|_{r'=0} = 0, \quad \text{and} \quad \ell(r' \rightarrow \infty) = \ell_0. \quad (21)$$

Eq. (20) is solved numerically using a shooting method, and Fig. 2 displays the obtained critical bubble profiles for increasing N .

The interface tension is well defined only at the critical temperature, and is given by

$$\sigma = T_c^3 \int_{-\infty}^{\infty} dz' \left[\frac{Z_\ell}{2} \left(\frac{d\ell}{dz'} \right)^2 + V'_{\text{eff}}(\ell, T_c) \right]. \quad (22)$$

At the critical temperature, the second term of (20) (replacing $r' \rightarrow z'$ as we are considering a planar wall) vanishes, and the resulting differential equation has a domain wall solution with $\ell(z' \rightarrow -\infty) = 0$ and $\ell(z' \rightarrow \infty) = \ell_0$. We can then rewrite (22) as

$$\sigma = T_c^3 \int_0^{\ell_0} d\ell' \sqrt{2Z_\ell V'_{\text{eff}}(\ell', T_c)}. \quad (23)$$

Most remarkably, (23) relates the surface tension, which is a static quantity measurable on the lattice, with the prefactor Z_ℓ of the kinetic term. The latter is a dynamic quantity and is therefore hard to access on the lattice. The relation (23) bridges this gap at least at the critical temperature. Determining the coefficient Z_ℓ by appropriately matching to lattice data of the interface tension is the significant improvement of this work in terms of deriving PLM parameters.

Lattice results have demonstrated that the pressure, $\Delta p = -\Delta V_{\text{eff}}$, scales as N^2 in the large- N limit. This justifies the assumption used in this work that we can access the large- N behaviour by a rescaling of the fitted Polyakov loop potential at the largest N accessible with the lattice. Here, we rescale the $N = 6$ potential, and we confirmed that the potential rescaled to $N = 8$ accurately matches the $N = 8$ lattice data. This demonstrates that $N = 6, 8$ are already in the large- N regime.

More accurately, we rescale the potential such that the large- N fit of the latent heat in (6) is matched. To ensure the PLM reproduces the exact values of the latent heat from the large- N fit for all $N > 6$, one must scale the effective potential in the following way:

$$V_{\text{eff}}^{N>6} = \left[\frac{0.360N^2 - 1.88}{0.360 \cdot 6^2 - 1.88} \right] \cdot V_{\text{eff}}^{N=6}. \quad (24)$$

If one were to scale the effective potential as $N^2/6^2$, at large N the PLM would estimate the latent heat to be a factor of ~ 0.85 smaller than the large- N fit of (6).

Using the above fact, one can obtain the large- N scaling of the interface tension from its expression in (23) for a given choice of Z_ℓ . If one would assume that the Polyakov loop has a canonical kinetic term ($Z_\ell = 1$), the interface tension would scale like $\sigma \propto N$ in the large- N limit. This disagrees with the observations of [14]. To recover the desired scaling, we set $Z_\ell = \delta N^2$, where δ is some coefficient to be tuned such that the interface tension from (23) agrees exactly with the results from the lattice, and is taken to be temperature-independent. The results

N	L/T_c^4	σ/T_c^3	$\delta(N)$
3	1.175(10)	0.0200(6)	0.14
4	3.8(2)	0.0997(76)	0.17
5	7.2(2)	0.258(11)	0.20
6	11.08(27)	0.461(29)	0.14
8	21.5(4)	0.994(47)	0.19
$\rightarrow \infty$	$0.360(6)N^2$	$0.0182(7)N^2$	$\rightarrow 0.24$

Table 2. Tabulated latent heats from [71] ($N = 3$) and [14] ($N = 4, 5, 6$, and 8) and interface tensions from [12] ($N = 3$) and [14] ($N = 4, 5, 6$, and 8), with corresponding δ -parameter from the Polyakov loop kinetic term obtained by matching the solution of (23) to the data for each N . While the interface tensions for $N = 3, 4, 5$, and 8 were matched to direct lattice results, that for $N = 6$ was equated to the large- N fit of (6).

in [14] of the direct computations of the interface tension for $N = 4, 5$, and 8 at infinite volume were used in this matching procedure, as well as that for $N = 6$ from the large- N fit of (6). In the case of $N = 3$, the infinite-volume computation of the interface tension from [12] was used. For $N > 8$, $\delta(N)$ was obtained by matching the large- N expression for the interface tension in (6) to (23) using the rescaled $N = 6$ effective potential, as is discussed above. The values of δ for each N are tabulated in Tab. 2. Remarkably, the parameter δ is an almost N -independent number of order one, which highlights that the N^2 factor captures most of the non-trivial scaling.

In summary, the Euclidean action used in this work then reads

$$S_3(T) = 4\pi T \int_0^\infty dr' r'^2 \left[\frac{\delta N^2}{2} \left(\frac{d\ell}{dr'} \right)^2 + V'_{\text{eff}}(\ell, T) \right]. \quad (25)$$

We have justified the introduction of $Z_\ell = \delta N^2$ in front of the kinetic term from considerations of the scaling of the interface tension with N . It is important to note that this scaling of the action, and thus the kinetic term, with N has been observed elsewhere in the literature [70], including in holographic studies of confinement [24–32] where it is a general feature. Crucially, the scaling of the action with N from the thin-wall approximation (7) is also in agreement.

C. Interface Tension and Latent Heat

We show that the Polyakov loop model accurately matches lattice observables, namely the interface tension and latent heat as a function of N . In Fig. 3, we plot the interface tension (left) and latent heat (right) against N , both from the large- N formulae of [14] and [12], and from the PLM. In both cases, the output of the PLM and lattice fitted formulae are in excellent agreement, particularly with the results of [14]. The fitting procedure and

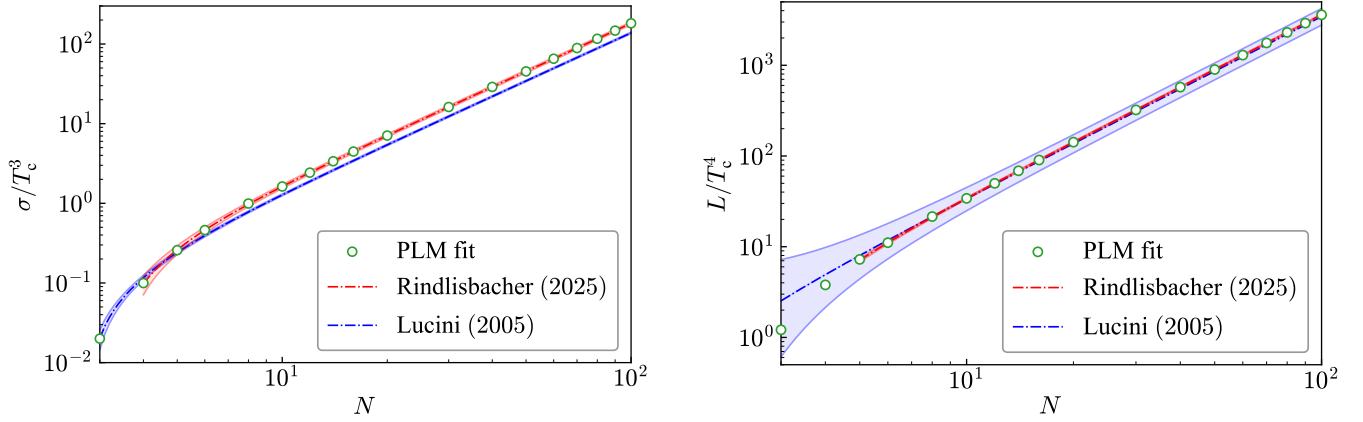


Figure 3. Interface tension in units of T_c^3 (left), and latent heat in units of T_c^4 (right), plotted as a function of the number of colours. The red and blue curves were drawn using large- N fits of the interface tension and latent heat obtained from two separate lattice computations, [14] and [12], respectively. The green points were calculated from the PLM fit using the formulae for the interface tension (23) and latent heat (4). Both of these quantities, by definition, were computed at the critical temperature.

δ -parameter tuning were employed with this goal in mind, and this acts as a check that the PLM can reproduce the thermodynamics of the phase transition. Note that the weaker agreement between the large- N fit of the latent heat and the PLM for $N = 3, 4$ and 5 is because the large- N fits are not applicable at small values of N , and are therefore not used.

By definition, both the interface tension and latent heat are computed at the critical temperature. Away from the critical temperature, the fitting procedure utilises the pressure and the trace of the energy-momentum tensor computed on the lattice [13]. Crucially, the $N = 3, 4, 5$, and 6 reconstructed effective potentials displayed similar behaviour around T_c , which gives some confidence that the effective theory correctly models the system dynamics at temperatures below T_c , at least for small N . As discussed later, there is greater uncertainty at large N .

Given the error estimates associated with the interface tension and latent heat computed on the lattice, the matching procedure described above allows for an upper- and lower-bound on the GW power spectrum to be obtained. Specifically, we re-fitted the effective potential by instead using the upper- and lower-bounds of the latent heat as the fitting constraint, giving effective potentials which reproduce these values. Then, we tuned δ to match the upper- and lower-bounds of the interface tension, in total giving four cases. In the results for the GW parameters, as described in Sec. IV, we represent the maximal and minimal values obtained from these four cases as an error bar.

IV. GW PARAMETERS

We outline the procedures undertaken to compute the stochastic GW background generated from a first-order

confinement phase transition in $SU(N)$ Yang-Mills theory, using the PLM introduced above. The GW power spectrum receives contributions from three independent sources: collisions of expanding bubbles [72–79], sound waves [46–48, 80, 81], and magnetohydrodynamic (MHD) turbulence [82–91]. In the case of thermal FOPTs such as those studied in this work, the contribution from sound waves dominates. We checked explicitly that this holds in our computation. Numerical simulations of GWs generated from acoustic sources were performed in [47], the results of which lead to the following fit:

$$h^2 \Omega_{\text{GW}}(f) = h^2 \Omega_{\text{GW}}^{\text{peak}} \left(\frac{f}{f_{\text{peak}}} \right)^3 \left(\frac{7}{4 + 3(f/f_{\text{peak}})^2} \right)^{7/2}, \quad (26)$$

where $h = H/(100 \text{ km/s/Mpc})$ is the dimensionless Hubble parameter. The peak frequency of the power spectrum, f_{peak} , is given by

$$f_{\text{peak}} = 1.9 \cdot 10^{-5} \text{ Hz} \left(\frac{\tilde{\beta}}{\xi_w} \right) \left(\frac{T_n}{100 \text{ GeV}} \right) \left(\frac{g_*}{100} \right)^{1/6}, \quad (27)$$

and the peak amplitude, $h^2 \Omega_{\text{GW}}^{\text{peak}}$, by

$$h^2 \Omega_{\text{GW}}^{\text{peak}} = 2.65 \cdot 10^{-6} \left(\frac{\xi_w}{\tilde{\beta}} \right) \left(\frac{\lambda_\alpha \kappa \alpha}{1 + \alpha} \right)^2 \left(\frac{100}{g_*} \right)^{1/3}, \quad (28)$$

see [50]. The nucleation temperature, T_n , effective number of relativistic degrees of freedom, g_* , inverse duration, $\tilde{\beta}$, bubble wall velocity, ξ_w , strength parameter, α , and efficiency factor, κ , are defined in the following sections. The computation of the GW power spectrum is thus reduced to a determination of each of these parameters. The term λ_α encodes the effect of the presence of visible matter on the observed power spectrum from the dark

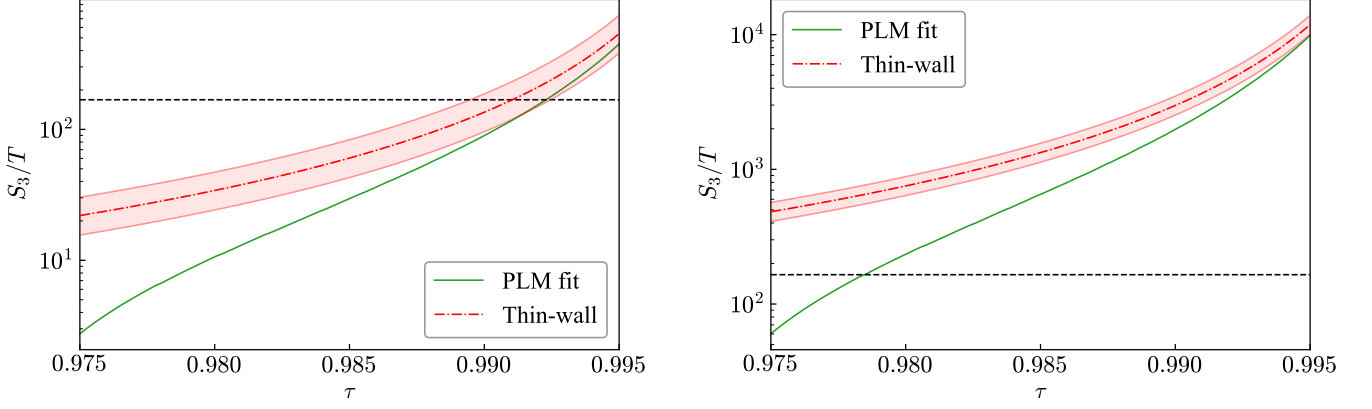


Figure 4. S_3/T plotted as a function of temperature for $N = 6$ (left) and $N = 20$ (right). The τ -axis runs from slightly above τ_{\min} to slightly below $\tau = 1$. The black dashed line represents the point at which the nucleation condition is met, $\Gamma/H^4 \sim 1$. For $N = 6$, the thin-wall approximation and the PLM fit show a reasonable agreement at the nucleation temperature, τ_n , while for $N = 20$, the thin-wall approximation is clearly breaking down.

sector phase transition, and is given by

$$\lambda_\alpha = \frac{g_*^{SU(N)}}{g_*} = \frac{g_*^{SU(N)}}{g_*^{\text{SM}} + g_*^{SU(N)}}. \quad (29)$$

In (29), g_*^{SM} denotes the Standard Model (SM) degrees of freedom, which are temperature dependent, and $g_*^{SU(N)} = 2 \cdot (N^2 - 1)$ denotes that from the $SU(N)$ dark sector. At large N , $g_*^{SU(N)} \gg g_*^{\text{SM}}$ and $\lambda_\alpha \simeq 1$. It is common in the literature for (29) to be absorbed in a redefinition of α [92–94].

To quantify the detectability of a GW signal, we employ the signal-to-noise ratio (SNR). At a detector with sensitivity curve $h^2\Omega_{\text{det}}(f)$, and $h^2\Omega_{\text{GW}}(f)$ defined in (26), the SNR is given by

$$\text{SNR} = \sqrt{\frac{T}{s} \int_{f_{\min}}^{f_{\max}} df \left(\frac{h^2\Omega_{\text{GW}}}{h^2\Omega_{\text{det}}} \right)^2}, \quad (30)$$

where T is the observation period of the detector in seconds. In this work, we take $T = 3$ years, and assume an $\text{SNR} > 1$ is detectable.

A. Nucleation Temperature, T_n

We use the nucleation temperature, T_n , to estimate the temperature of GW production. The nucleation temperature is defined to be the temperature at which the bubble nucleation rate, Γ , per Hubble volume per Hubble time is approximately equal to one [50], i.e., $\Gamma/H^4 \sim 1$, with [54]

$$\Gamma(T) = T^4 \left(\frac{S_3(T)}{2\pi T} \right)^{3/2} e^{-S_3(T)/T}. \quad (31)$$

The Hubble parameter is obtained from the Friedmann equation under the assumption that the transition occurs

in the radiation-dominated era,

$$H(T) = \sqrt{\frac{\pi^2 g_*}{90}} \frac{T^2}{M_{\text{P}}}. \quad (32)$$

Above, $M_{\text{P}} = 2.435 \cdot 10^{18}$ GeV is the reduced Planck mass. In general, a more accurate definition of the temperature of GW production is the percolation temperature, T_p [95, 96]. However, since in our case the FOPT occurs rapidly, $T_p \simeq T_n$ holds and the nucleation temperature is a sufficient estimate.

From (31), the quantity of primary importance in the determination of T_n is S_3/T . In Fig. 4, we plot S_3/T for $N = 6$ and $N = 20$ against τ , with

$$\tau = T/T_c, \quad (33)$$

using both the thin-wall approximation and the PLM. Near the critical temperature, these curves are in agreement, as one would expect given that the critical bubble configuration is thin for temperatures just below T_c . Since it diverges both at $T = 0$ and $T = T_c$, the thin-wall formula for S_3/T from (5) has a minimum at some temperature in the range $0 < T < T_c$. Conversely, the fitted Polyakov loop effective potentials from (17) exhibit a temperature $0 < T_{\min} < T_c$ at which S_3/T vanishes. This is the temperature below which the deconfined phase no longer exists as a metastable state. As in the thin-wall approximation, S_3/T from the PLM also diverges at $T = T_c$, and it is therefore a monotonically increasing function of T . This demonstrates that the curves in Fig. 4 have to disagree at lower temperatures.

To show that the thin-wall approximation breaks down in the large- N limit, we highlight two pieces of evidence. Firstly, consider the profile of the PLM critical bubble as N increases in Fig. 2. From the scaling of the interface tension, which resulted in a kinetic term scaling with N^2 , the three-dimensional action of (25) scales as N^2 . To satisfy $\Gamma/H^4 \sim 1$, the nucleation temperature must decrease

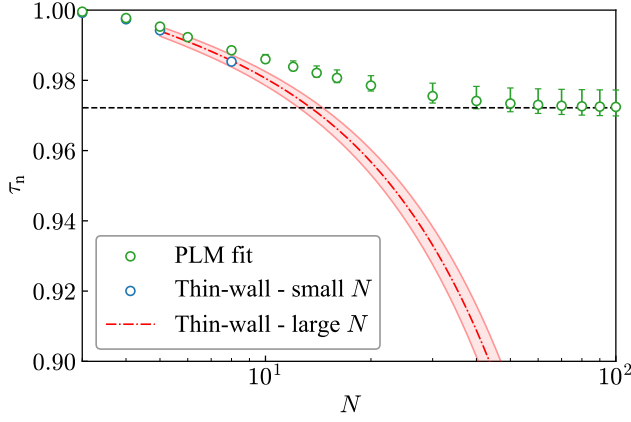


Figure 5. Nucleation temperature, in units of the critical temperature ($T_c = 1$ GeV), plotted as a function of the number of colours. The red curve was obtained using the thin-wall approximation, see (7). The blue points were obtained using the thin-wall formula (5) and the infinite-volume extrapolated values of the interface tension and latent heat given in [14]. The green points are the nucleation temperatures computed directly from the PLM. The black dashed line displays the temperature at which the barrier disappears for the $N \geq 6$ effective potentials, $\tau_{\min}^{N=6}$.

with N , see Fig. 4. With greater supercooling, the critical bubble configuration decreases in radius, and the wall thickens. In this picture, the thin-wall approximation is rendered obsolete as the Euclidean action simply cannot be approximated by contributions from an infinitesimal wall and the bulk volume.

Even without the knowledge of the critical bubble profiles, one can still show that the thin-wall approximation breaks down at large N . The thin-wall formula for S_3/T scales as N^2 in the large- N limit, just like in the PLM; however, unlike that from the PLM, it is not a monotonically increasing function of temperature. As discussed above, it has a minimum between $T = 0$ and $T = T_c$. Therefore, as N is increased, a point will be reached at which S_3/T (as a function of temperature) never falls low enough for the nucleation condition to be met. Here, it was found to be in the region around $N \simeq 170$. This logic is displayed in Fig. 4, where the black horizontal line denotes the value of S_3/T at which $\Gamma/H^4 \sim 1$. For $N = 6$, this line intersects the two S_3/T curves at approximately the same temperature, whereas at $N = 20$ there is a larger discrepancy in the prediction for the degree of supercooling. If one were to plot S_3/T for $N \gtrsim 170$, the thin-wall curve would never intersect the black line. The conclusion is that, while the thin-wall approximation may be valid for small values of N , the large- N behaviour of GW parameters derived using this approximation should not be trusted. In Secs. IV B and V, we state more definitively the values of N for which thin-wall is valid.

Using a critical temperature of $T_c = 1$ GeV, the PLM and thin-wall predictions for the nucleation temperature are plotted as a function of N in Fig. 5. For the reasons

N	τ_{\min}	τ_n
3	$0.99518^{+2 \cdot 10^{-5}}_{-4.7 \cdot 10^{-4}}$	$0.99931^{+5 \cdot 10^{-5}}_{-3 \cdot 10^{-5}}$
4	$0.99205^{+1.27 \cdot 10^{-3}}_{-1.26 \cdot 10^{-3}}$	$0.99774^{+2.7 \cdot 10^{-4}}_{-2.5 \cdot 10^{-4}}$
5	$0.98664^{+1.42 \cdot 10^{-3}}_{-1.46 \cdot 10^{-3}}$	$0.99530^{+2.5 \cdot 10^{-4}}_{-2.5 \cdot 10^{-4}}$
6	$0.97219^{+2.61 \cdot 10^{-3}}_{-4.92 \cdot 10^{-3}}$	$0.99230^{+9.9 \cdot 10^{-4}}_{-8.1 \cdot 10^{-4}}$
8	$\tau_{\min}^{N=6}$	$0.98855^{+9.7 \cdot 10^{-4}}_{-7.0 \cdot 10^{-4}}$
$\rightarrow \infty$	$\tau_{\min}^{N=6}$	$\rightarrow \tau_{\min}$

Table 3. Minimum and nucleation temperatures, with associated upper- and lower-error bars, for $N = 3, 4, 5, 6, 8$, and $N \rightarrow \infty$ from the reconstructed PLM. The nucleation temperatures were computed using $T_c = 1$ GeV, while the minimum temperatures are independent of this choice.

outlined above, at small values of N , the two approaches are in agreement. With increasing N , the results differ by a greater degree. A notable feature of the nucleation temperatures obtained from the PLM is that they quickly approach $\tau_{\min}^{N=6} \simeq 0.972$, denoted by the black dashed line. In the large- N limit, the amount of supercooling is therefore bounded by this value and can be thought of as approximately constant. The constant nucleation temperature at large N allows one to estimate the large- N scaling of other GW parameters such as the inverse duration, $\hat{\beta}$, and bubble wall velocity, ξ_w , as discussed in Secs. IV B to IV E and V. For small values of N , and as $N \rightarrow \infty$, these nucleation temperatures are tabulated alongside the corresponding minimum temperature of the deconfined phase in Tab. 3.

For each value of N plotted in Fig. 5, the nucleation temperature was also computed at a critical temperature of $T_c = 100$ GeV. The result was a marginal reduction in $\tau_n(N)$ (i.e. increased supercooling) when compared to that computed at $T_c = 1$ GeV across the entire range of N used. This became increasingly negligible at large N as $\tau_n \rightarrow \tau_{\min}$.

At large N , the greatest source of uncertainty in the nucleation temperature stems from the rescaling procedure using the $SU(6)$ effective potential displayed in (24), which sets the limit on supercooling to be $\tau_{\min}^{N=6}$ in the large- N limit. This rescaling works under the assumption that $N = 6$ is already large, such that one would not expect $\tau_{\min}^{N=6}$ to decrease much with an increase in N . In the holographic model of [26], which is strictly valid for large N , a similar minimum temperature was observed to this $SU(6)$ effective potential. That being said, the lack of lattice data for $N > 8$ rendered this approximation a necessity to access the large- N behaviour. The implications of this for each parameter entering the formula for the GW power spectrum in (26) are discussed in detail in Secs. IV F and V C. Notably, the maximal degree of supercooling for $N \geq 3$ was estimated in [57], where a

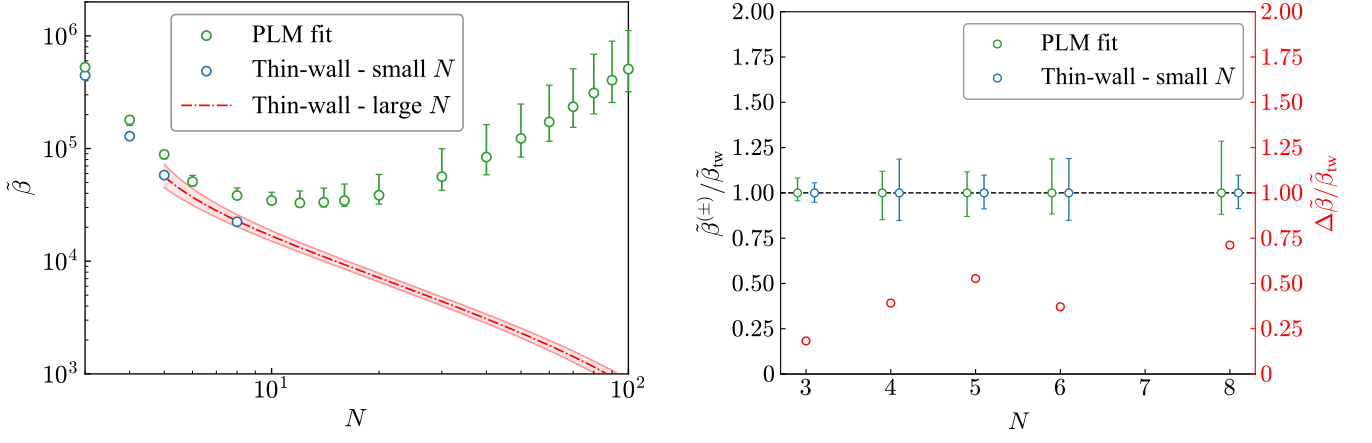


Figure 6. Inverse duration of the phase transition, in units of the Hubble parameter, plotted as a function of the number of colours. In the left-hand panel, the inverse duration is plotted at large N ; the red curve is the result obtained through the thin-wall approximation in (7), and that computed using the PLM fit is plotted in green. The right-hand panel displays the inverse duration at small N , where thin-wall predictions for $N = 3, 4, 5$, and 8 were made using infinite-volume-extrapolated values of the interface tension and latent heat instead of large- N fits (and shown in the left-hand panel in blue). The left y -axis, $\tilde{\beta}^{(\pm)}/\tilde{\beta}_{\text{tw}}$, denotes the relative error in the inverse duration. The right y -axis gives the fractional difference between the inverse duration from the PLM and the thin-wall. The critical temperature was set to $T_c = 1$ GeV in both cases.

slightly larger value was obtained.

B. Inverse Duration, $\tilde{\beta}$

Next, we examine the phase transition inverse duration, β . With the bubble nucleation rate defined in (31), the inverse duration is written as [91],

$$\beta \equiv \left. \frac{d}{dt} \log \Gamma(t) \right|_{t=t_n}, \quad (34)$$

where the nucleation time, t_n , is taken to be the time of GW production. For a sufficiently fast phase transition (i.e. $\beta \gg H$), the nucleation rate can be approximated by

$$\Gamma(t) \simeq \Gamma(t_n) e^{\beta(t-t_n)}. \quad (35)$$

A Taylor expansion of S_3 in (31) around $t = t_n$ allows for the identification

$$\beta = - \left. \frac{d}{dt} \frac{S_3(T)}{T} \right|_{t=t_n}. \quad (36)$$

In practice, the inverse duration is made dimensionless by dividing by H . Using that $dT/dt = -HT$,

$$\tilde{\beta} \equiv \frac{\beta}{H(T_n)} = T \left. \frac{d}{dT} \frac{S_3(T)}{T} \right|_{T=T_n}. \quad (37)$$

From the Euclidean action in the thin-wall approximation (7), the inverse duration can be computed analytically, whereas that using the PLM must be obtained numerically. In Fig. 6, the dimensionless inverse duration computed using both the thin-wall approximation and the PLM

is plotted as a function of the number of colours at a critical temperature of $T_c = 1$ GeV. For small values of N (≤ 6), the two approaches are in good agreement, as is demonstrated in the right-hand panel; this can be attributed both to the matching procedure described in Sec. III B and to the relatively small degree of supercooling. Indeed, as N increases from 3 to 8, the greater discrepancy in supercooling begins to take hold and the estimates of $\tilde{\beta}$ disagree more strongly. In the left-hand panel of Fig. 6, the inverse duration from the PLM is plotted for a larger range of N , and is accompanied by the prediction made using the thin-wall formula of (7).

At large N , the inverse durations computed in the thin-wall approximation and using the PLM are in disagreement. Although the interface tension and latent heat derived from the Polyakov loop potential exactly agree with the lattice large- N fits, the discrepancy in the observed supercooling of Fig. 5 takes over and the predictions for $\tilde{\beta}$ begin to mutually diverge. For the reasons outlined in Sec. IV A, the thin-wall computation should not be trusted in this regime. A striking result in the PLM is the observation of a turning point in $\tilde{\beta}$ at $N \simeq 12$ (notably, the same behaviour was observed in [38] at $N \simeq 11$ for different reasons). As discussed in Sec. V, this feature has a significant effect on the behaviour of the peak amplitude and peak frequency of the GW power spectrum as a function of N . It should be noted that the asymmetry in the error bars stems from the corresponding asymmetric error in the nucleation temperature.

In the large- N regime, one would naively expect that the inverse duration scales as N^2 . The reason is that the effective potential scales with N^2 , see (24), and so does the three-dimensional Euclidean action S_3 . Other N dependences can arise from the N dependence of the

nucleation temperature τ_n , which is, however, approximately constant at large N . In rough agreement with this expectation, we find numerically that $\tilde{\beta} \propto N^{2.12}$ for $N \geq 60$. The small discrepancy arises due to the nucleation temperature being only approximately constant. The large- N power-law fit parameter of the inverse duration is displayed in Tab. 4 in Sec. V A for $T_c = 1$ GeV and $T_c = 100$ GeV, where we discuss the implications on the GW power spectrum peak amplitude.

The inverse duration of the phase transition was also computed at a critical temperature of $T_c = 100$ GeV for each N . The effect was to slightly scale down $\tilde{\beta}$ by a factor which became increasingly negligible as the nucleation temperature approached τ_{\min} (i.e. as N became large). The turning point in $\tilde{\beta}$ remained at $N \simeq 12$.

Looking ahead, we will see that the inverse duration is the dominating quantity in the prediction of the GW power spectrum. Across the entire range of N it has a large magnitude, which generally suppresses the spectrum, and its shape as a function of N greatly influences the shape of the peak amplitude with N . The reason for such a large $\tilde{\beta}$ can be attributed to the rapidly changing effective potential with temperature, which in turn causes the Euclidean action to vary steeply. The physical picture is that below the critical temperature, a large number of very small true vacuum bubbles nucleate in the gluon plasma ($\beta \sim 1/R$). These bubbles expand, collide, and generate sound waves in this plasma, but due to the small radii, we expect the resulting GW signal to be weak.

C. Bubble Wall Velocity, ξ_w

The non-perturbative nature of first-order confinement phase transitions renders the computation of the bubble wall velocity a formidable task. Indeed, it has often been left as a free parameter [34, 36–42], introducing a significant degree of uncertainty in the resulting GW power spectrum. More recently, progress has been made in the determination of the bubble wall speed in strongly coupled transitions, particularly through the use of holographic models [97–100]. In this work, we follow [52], which develops a framework to estimate the wall speed in theories that experience a large change in the number of degrees of freedom across the phase transition, in a model-independent way. The $SU(N)$ Yang-Mills theory lies within this regime, particularly in the large- N limit.

A review of the hydrodynamics related to computing the bubble wall speed can be found in [101]. The imposition of conservation of energy-momentum across the phase transition boundary allows one to derive the following matching conditions (under the assumption that the outward-moving wall is infinitesimally thin, which is a good approximation in most cases):

$$\begin{aligned} w_+ v_+^2 \gamma_+^2 + p_+ &= w_- v_-^2 \gamma_-^2 + p_-, \\ w_+ v_+^2 \gamma_+^2 &= w_- v_-^2 \gamma_-^2, \end{aligned} \quad (38)$$

where a $+$ ($-$) denotes evaluation just ahead of (behind) the bubble wall, $w_{\pm} = T \partial p_{\pm} / \partial T$ is the enthalpy, v_{\pm} represents the fluid velocity in the wall frame, and $\gamma_{\pm} = 1/\sqrt{1 - v_{\pm}^2}$. The following can then be obtained:

$$v_+ v_- = \frac{p_+ - p_-}{e_+ - e_-}, \quad \text{and} \quad \frac{v_+}{v_-} = \frac{e_- + p_+}{e_+ + p_-}. \quad (39)$$

The hydrodynamic equations admit three classes of solutions:

- (I) Deflagration: the fluid is at rest behind the wall ($v_- = \xi_w$). A shock is present, ahead of which the temperature is equal to the nucleation temperature ($T_{\text{sh}}^+ = T_n$).
- (II) Detonation: the fluid is at rest in front of the wall ($v_+ = \xi_w$). No shock is present, and the temperature in front of the wall is the nucleation temperature ($T_+ = T_n$).
- (III) Hybrid: a superposition of the above solutions. The fluid velocity behind the wall is equal to the speed of sound in the low-temperature phase ($v_- = c_{s-}$). A shock is present, ahead of which the temperature is equal to the nucleation temperature ($T_{\text{sh}}^+ = T_n$).

To proceed, one must find a way to relate v_+ to v_- , or equivalently T_+ to T_- . In the presence of a plasma, the bubble wall quickly reaches a terminal velocity; to obtain the relation between \pm quantities in full generality requires an analysis of the friction forces on the wall. As was alluded to above, this is a challenging task, particularly for strongly coupled theories. Another approach is to compute an upper- and lower-bound on the wall velocity, and treat it as a free parameter in this band. For a discussion of these limits, see [102].

In [52], a large jump in enthalpy is imposed by the suppression of quantities in the low-enthalpy (confined) phase by N^2 in the matching conditions of (38) and (39). Through considerations of the scaling of these matching conditions in the large- N limit, the following constraints were derived:

$$T_+ = T_c, \quad \text{and} \quad v_+ = 0. \quad (40)$$

The above conditions agree with the results of the holographic simulations in [97, 100], and allow one to forgo the use of bounds on the wall velocity. Clearly, the second constraint implies the exclusion of detonations. Using (40), the hydrodynamics equations were solved in [52] for the strongly coupled holographic model presented in [26] to obtain the bubble wall speed as a function of the nucleation temperature. Importantly, this holographic model exhibits similar behaviour to the PLM regarding the limit on supercooling, and one would therefore expect similar predictions for the sound speed and bubble wall speed in this work. Both models make thermodynamic predictions only of the high-enthalpy phase, which here is

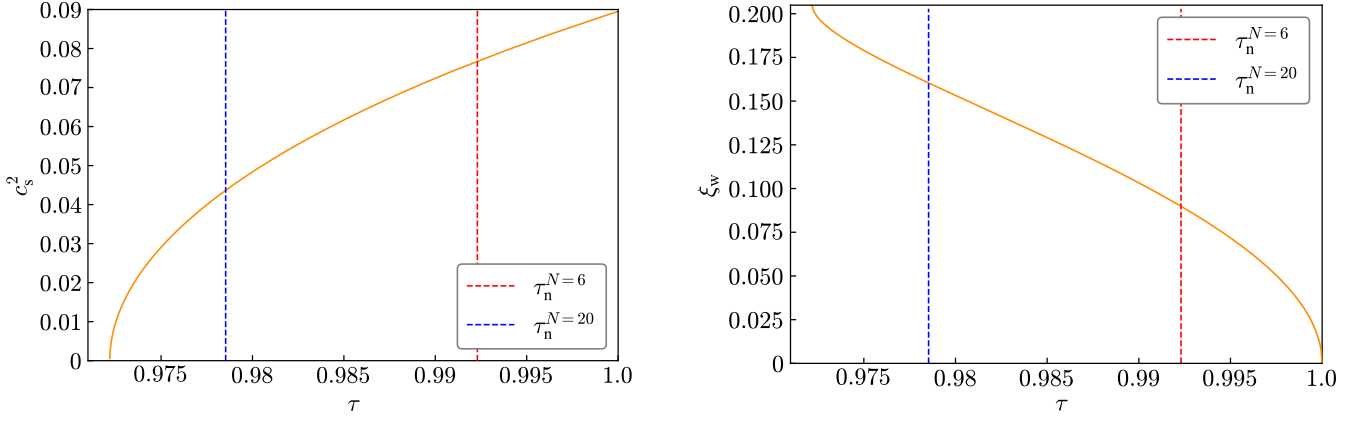


Figure 7. Squared sound speed of the high-enthalpy phase (left) and bubble wall velocity (right) as a function of the temperature ($\tau_{\min} \leq \tau \leq 1$). The curves were obtained for $N \geq 6$ and $T_c = 1$ GeV. The nucleation temperatures for $N = 6$ and $N = 20$ are indicated with vertical dashed lines.

the deconfined phase, but the large- N conditions (40) allow the computation of the wall speed to proceed without any knowledge of the fluid variables behind the bubble wall.

Thermodynamics tells us that the sound speed is given in terms of the pressure and energy density, e , as:

$$c_s^2 \equiv \frac{\partial p}{\partial e} = \frac{\partial p / \partial T}{\partial e / \partial T}, \quad e = T \frac{\partial p}{\partial T} - p, \quad (41)$$

which we evaluate at ℓ_0 for the deconfined phase, i.e. $p = p_+ \simeq -V_{\text{eff}}(\ell = \ell_0, T)$. More precisely, the PLM only gives us access to $\Delta p \simeq -(V_{\text{eff}}(\ell = \ell_0, T) - V_{\text{eff}}(\ell = 0, T))$ and it implicitly sets $p_- = 0$. Under the assumption that the absolute pressure p_+ is shifted by a constant, this drops out of the temperature derivatives in (41). Using (41), the sound speed was computed from the reconstructed Polyakov loop potentials, the result of which is plotted on the left-hand side of Fig. 7 for $N \geq 6$. Qualitatively, the sound speed curve is in good agreement with that obtained from the dark $SU(N)$ holographic model of [26], differing by a small amount at the critical temperature. This stems from a slight discrepancy in the prediction for τ_{\min} . At large T compared to the critical temperature, the speed of sound in the deconfined phase approaches its conformal value of $c_s \simeq 1/\sqrt{3}$ as required.

Employing the large-enthalpy-jump conditions (40), the hydrodynamics of the confinement transition in the PLM were solved. The bubble wall speed for $N \geq 6$ is plotted on the right-hand side of Fig. 7 as a function of temperature ($T_{\min} \leq T \leq T_c$). As expected, given the similarities in the predicted sound speed and the limit on supercooling between the PLM and the holographic model of [26], the bubble wall velocity curves are in good qualitative agreement. Here, a maximum wall velocity of $\xi_w \simeq 0.20$ is observed, which can be thought of as the limiting value of ξ_w that is approached at large N . Using the model in [26], a maximum value of $\xi_w \simeq 0.25$ was obtained in [52], which can be explained by the slightly

lower minimum temperature when compared to the PLM.

Strictly speaking, the right-hand-side plot of Fig. 7 actually displays the solution for v_- as a function of temperature below the critical, which only equates to the wall speed for a deflagration [101]. In this case, the fluid is at rest inside the bubble such that $v_- = \xi_w$. While the large-enthalpy limit excludes detonations, made explicit by the conditions of (40), hybrid solutions remain allowed. For hybrids, $v_- = c_{s-}$ and $c_{s-} < \xi_w < v_{\text{CJ}}$, where v_{CJ} is the Chapman-Jouguet velocity; the minimum wall speed of a detonation. With knowledge of the sound speed in the confined phase, one should then compute the wall velocity through a shooting method. As is stated above, the PLM gives us no information on the sound speed in the low-enthalpy phase. We therefore assume that it quickly returns to that of a relativistic ideal gas with $c_{s-} = 1/\sqrt{3}$, implying deflagration solutions only. Under this assumption, $v_- = \xi_w$ and the right-hand side of Fig. 7 is indeed the wall velocity.

Notably, in the holographic study of the bubble wall velocity in [97], the sound speed in the low-enthalpy phase was successfully computed. It was found to intersect that of the deconfined phase at $T = T_c$ and quickly tend towards the conformal value with decreasing temperature. Given a suitable equation of state describing the low-enthalpy phase, it is reasonable to assume that similar behaviour would be observed using the PLM. In this case, the confined sound speed, c_{s-} , would be bounded by $c_{s+}^2(T = T_c) \simeq 0.09 \leq c_{s-}^2 \leq 1/3$, admitting only deflagrations as before (since $c_{s-} \geq \sqrt{0.09} > v_- = \xi_w$ by Fig. 7).

We would like to point out a potential source of confusion. The curves of the sound speed in the deconfined phase and the wall velocity intersect at some temperature, see Fig. 7. Naively, this would imply that the bubble wall moves outwards with a speed greater than the sound speed of the plasma, such that in this regime we actually find detonations. This would be in contradiction to the

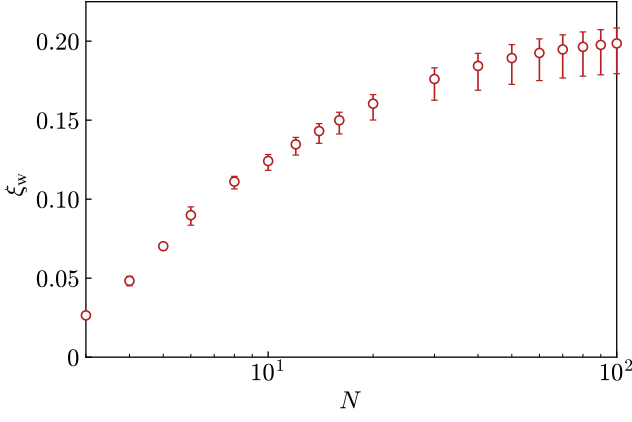


Figure 8. Bubble wall velocity evaluated at the nucleation temperature and plotted as a function of N for $T_c = 1$ GeV.

second large-enthalpy-jump condition in (40) used in the computation. The contradiction is resolved by recalling the presence of a shock front in which reheating of the plasma occurs, and that the first of the large-enthalpy-jump conditions in (40) implies this plasma is reheated up to the critical temperature in front of the bubble wall. Therefore, the bubble wall interacts with a plasma of sound speed $c_{s+}(T_c)$ and detonations are indeed excluded, given that the wall velocities we compute never exceed this value.

These considerations lead us to the predictions of the bubble wall velocity from the PLM as a function of N displayed in Fig. 8. The wall velocity is monotonically increasing and approaches $\xi_w \simeq 0.20$ at large N . The small value of ξ_w at small N provides an additional suppression of the GW power spectrum at small N .

D. Phase Transition Strength Parameter, α

The total energy available to be converted into GWs is given by the change in the trace of the energy-momentum tensor across the phase transition. In this work, we define the dimensionless phase transition strength parameter, α , in terms of the trace anomaly, θ , which is proportional to the trace of the energy-momentum tensor. In terms of the pressure and energy density, the trace anomaly is given by

$$\theta_{\pm} = \frac{1}{4} (e_{\pm} - 3p_{\pm}). \quad (42)$$

Defining $\Delta\theta = \theta_+ - \theta_-$, which therefore encodes the energy available for conversion to shear stress, the strength parameter is written as

$$\alpha = \frac{4}{3} \frac{\Delta\theta}{w_+} \Big|_{T=T_n}, \quad (43)$$

where w_+ quantifies the degrees of freedom in the deconfined phase.

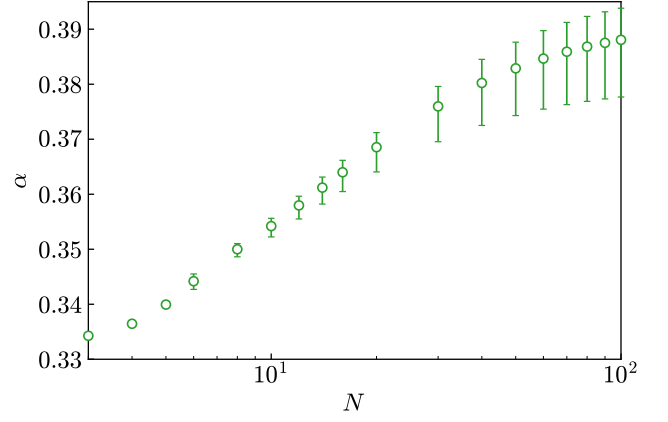


Figure 9. Phase transition strength parameter, calculated from (43) at $T_c = 1$ GeV, plotted as a function of N .

To access the pressure, we use $p_{\pm} \simeq -V_{\text{eff}}(\ell_{\pm}, T) \equiv -V_{\text{eff}\pm}$, where ℓ_{\pm} denotes $\ell = \ell_0$ and $\ell = 0$ respectively. The potential is normalised to $V_{\text{eff}}(\ell = 0, T) = 0$, which allows one to express (42) in terms of quantities evaluated in the deconfined phase:

$$\alpha = \frac{1}{3} \frac{T \partial V_{\text{eff}+} / \partial T - 4V_{\text{eff}+}}{T \partial V_{\text{eff}+} / \partial T} \Big|_{T=T_n}. \quad (44)$$

For transitions which occur at $T_n \simeq T_c$, such that $V_{\text{eff}+} \simeq 0$, we find $\alpha \simeq 1/3$, see also [36, 38, 39, 41]. Therefore, given the nucleation temperatures plotted in Fig. 5, one expects $\alpha \simeq 1/3$ for small values of N , and that at large N the strength parameter should asymptotically approach some value, given that the nucleation temperature remains approximately constant ($\simeq \tau_{\text{min}}^{N=6}$). We show the transition strength parameter in Fig. 9, and in the large- N limit it approaches $\alpha \simeq 0.39$.

E. Efficiency Factor, κ

The final quantity to be defined, which enters the computation of the GW power spectrum (26), is the efficiency factor. In our definition, we split up κ into

$$\kappa = \sqrt{\tau_{\text{sw}}} \kappa_{\text{sw}}, \quad (45)$$

where τ_{sw} encodes the lifetime of the source, and κ_{sw} is the usual efficiency factor. The efficiency factor is defined as the ratio of the total kinetic energy in the plasma to the vacuum energy, and is therefore a measure of the total energy fraction which can go into GW production; the rest is used to increase the thermal energy of the system. Its definition reads,

$$\kappa_{\text{sw}} = \frac{3}{\epsilon \xi_w^3} \int d\xi w(\xi) v(\xi)^2 \gamma(\xi)^2 \xi^2, \quad (46)$$

where ϵ is the vacuum energy released in the transition, γ is the Lorentz factor, w is the enthalpy, and ξ is a

coordinate in the frame of the bubble centre. To obtain the efficiency factor in full generality requires the fluid velocity profile, $v(\xi)$, which can be computed by integrating the fluid equations, as is discussed in [101], and one should include the temperature-dependent sound speed. This is particularly relevant where it deviates strongly from the conformal value, such as in the present scenario.

In situations where the hydrodynamics is not precisely known, it is simpler to use fitted formulae for κ_{sw} from numerical simulations [101]. Relevant in this study, given the wall velocity is bounded to be a deflagration, are the following:

$$\begin{aligned}\kappa_A &\simeq \xi_w^{6/5} \frac{6.9\alpha}{1.36 - 0.037\sqrt{\alpha} + \alpha}, & \xi_w &\ll c_s, \\ \kappa_{A \rightarrow B} &\simeq \frac{c_s^{11/5} \kappa_A \kappa_B}{\left(c_s^{11/5} - \xi_w^{11/5}\right) \kappa_B + \xi_w c_s^{6/5} \kappa_A}, & \xi_w &\lesssim c_s, \\ \kappa_B &\simeq \frac{\alpha^{2/5}}{0.017 + (0.997 + \alpha)^{2/5}}, & \xi_w &= c_s,\end{aligned}\quad (47)$$

where $c_s \equiv c_{s+}(T_+ = T_c)$ is understood. Given the assumption of a constant sound speed, the use of the above formulae should be taken as a conservative estimate of κ_{sw} . We expect the efficiency factor in a full calculation to be larger and we reserve this investigation for a future study.

In the computation of the GW power spectrum, we choose the appropriate fit for the efficiency factor for each value of N depending on the value of the wall velocity displayed in Fig. 8. Specifically, we choose: (i) $\xi_w < 0.25 c_s \implies \kappa_{\text{sw}} = \kappa_A$, and (ii) $0.25 c_s \leq \xi_w < c_s \implies \kappa_{\text{sw}} = \kappa_{A \rightarrow B}$. Since the wall velocity is lower at small N , the efficiency factor κ_{sw} further suppresses the GW spectrum at small N .

To determine the GW power spectrum from an acoustic source, one must also take into account the lifetime of this source [81]. We introduce a factor of $\sqrt{\tau_{\text{sw}}}$, the length of the sound wave production period, in the definition of κ (45). The amplitude of the power spectrum therefore grows linearly with the source duration as $h^2 \Omega_{\text{GW}}^{\text{peak}} \propto \kappa^2$. In an expanding universe, this factor is given by [103]

$$\tau_{\text{sw}} = 1 - \left[1 + 2 \frac{(8\pi)^{1/3} \xi_w}{\tilde{\beta} U_f} \right]^{-1/2}, \quad (48)$$

which acts to significantly suppress the peak amplitude of the spectrum. In (48), U_f denotes the root-mean-squared fluid velocity, which takes the following form:

$$U_f^2 \simeq \frac{3}{\xi_w(1+\alpha)} \int_{c_s}^{\xi_w} d\xi \frac{\xi^2 v(\xi)^2}{1-v(\xi)} \simeq \frac{3}{4} \frac{\alpha}{1+\alpha} \kappa_{\text{sw}}. \quad (49)$$

Notably, in the simulations of [104] it was found that the GW amplitude continued to grow after τ_{sw} (which

strictly speaking denotes the timescale over which nonlinearities develop, but can be thought of as that beyond which efficient sound wave generation ceases), albeit much slower than linearly. In this sense, the introduction of τ_{sw} into the formula for the GW power spectrum in (26), which enforces that the source is abruptly turned off at this point, is a lower-bound on the timescale of GW production from sound waves. However, given the slowly-growing amplitude after τ_{sw} with time, this likely remains a reasonable estimate.

F. GW Parameters at Large N

Above, we have displayed the results for each parameter that enters the formula of the GW power spectrum (26). Here, we discuss the observed large- N scaling of these parameters and the uncertainties in the large- N limit.

The PLM fitting is based upon lattice data at and around the critical temperature. Consequently, properties further away from the critical temperature have a larger uncertainty. As such, the minimum temperature τ_{min} where the potential barrier disappears has a rather large uncertainty in our fitting procedure. Additionally, we use the rescaled $N = 6$ data to determine the large- N Polyakov loop potential and hence $\tau_{\text{min}}^{N=6} \simeq \tau_{\text{min}}^{N \rightarrow \infty}$. While we expect the minimum temperature of the deconfined phase in $SU(N)$ to tend to a constant in the large- N limit, it could be lower than that for $SU(6)$. This leads to an additional uncertainty in the GW parameters at large N , which is not quantified in their error bars. We discuss the implications of a lower $\tau_{\text{min}}^{N \rightarrow \infty}$ in the following.

The inverse duration displayed in Fig. 6 scales as $N^{2.12}$ for $N \geq 60$ as discussed in Sec. IV B. If τ_{min}^N does continue to decrease beyond that at $N = 6$, the greater degree of supercooling would cause S_3/T to vary less steeply with temperature than is observed for $N = 6$ in Fig. 4, leading $\tilde{\beta}$ to be slightly suppressed for larger values of N . The turning point in the inverse duration would then be pushed to a larger N , and so too would the onset of the approximate N^2 scaling. In the case of a lower $\tau_{\text{min}}^{N \rightarrow \infty}$, we therefore would expect $\tilde{\beta}$ to be shifted downwards for $N \geq 6$.

The wall velocity in the PLM approaches $\xi_w \simeq 0.20$ at large N , see Fig. 8. In Sec. IV C, we argued that this is due to τ_{min} approaching a constant at large N , and the value of $\tau_{\text{min}}^{N \rightarrow \infty}$ provides the largest uncertainty on the wall velocity. If τ_{min} saturates at a smaller value, then the wall velocity approaches a larger value, and the shape of the curve would be similar to that found here. Due to the comparison with [52], where a maximum value of $\xi_w \simeq 0.25$ was found, we are confident that we have presented a reasonable estimate of the wall velocity at large N .

The phase transition strength parameter plotted in Fig. 9 tends towards a constant value in the large- N limit. This is explained by the presence of a minimum temperature of the deconfined phase, which limits the

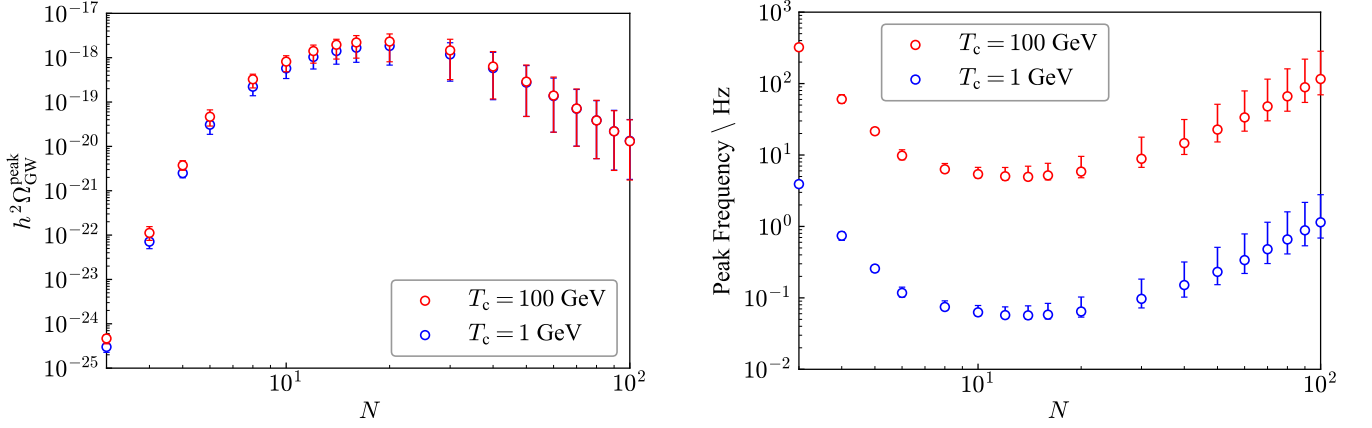


Figure 10. Peak amplitude (left) and peak frequency (right) of the computed stochastic GW background, plotted as a function of the number of colours, shown for both $T_c = 1$ GeV and $T_c = 100$ GeV.

degree of supercooling. If $\tau_{\min}^{N \rightarrow \infty}$ was lower than that at $N = 6$, the strength parameter would approach a slightly larger value than was found here. This would have a minimal effect.

Overall, the GW parameter with the largest uncertainty at large N is the inverse duration, which in turn is dominated by the uncertainty on the minimum temperature τ_{\min} at large N . While we are confident that we have correctly captured the large- N scaling, the value at which the scaling sets in could be at slightly larger N .

V. GW SPECTRUM

We have displayed and discussed in [Sec. IV](#) the results for each parameter contributing to the GW power spectrum (26). In this section, we discuss the features of the resulting GW spectra and quantify their detectability at future GW observatories through the signal-to-noise ratio.

A. Peak Amplitude and Frequency

We display the peak amplitude of the GW power spectrum, $h^2 \Omega_{\text{GW}}^{\text{peak}}$, as a function of N in the left panel of [Fig. 10](#). The peak amplitude has a maximum at $N \simeq 20$ but has a small value overall, $\mathcal{O}(10^{-24})$ for $N = 3$ and $\mathcal{O}(10^{-18})$ at the maximum. Qualitatively, the peak amplitude of the GW power spectrum is a mirror image of the $\tilde{\beta}$ curve in [Fig. 6](#), which is the most important parameter for this quantity. Note that the extremum is shifted slightly to larger N , from $N \simeq 12$ in the $\tilde{\beta}$ curve, to $N \simeq 20$ in $h^2 \Omega_{\text{GW}}^{\text{peak}}$. This is due to the wall velocity, the strength parameter, and the efficiency factor increasing steadily with N .

In [Fig. 10](#), the peak amplitude is plotted for both $T_c = 1$ GeV and $T_c = 100$ GeV. The slight variation in $h^2 \Omega_{\text{GW}}^{\text{peak}}$ between each T_c is as a result of the slightly

different nucleation temperatures ($\tau_n = T_n/T_c$) obtained from (31). This effect is minimal due to the exponential suppression of the bubble nucleation rate (31) by S_3/T and Planck suppression of T_c . The differences between τ_n , and therefore the peak amplitudes, for each critical temperature generally shrink with N . Again, this is due to the fact that the dimensionless nucleation temperature approaches τ_{\min} irrespective of the critical temperature used in the computation.

At large N , the peak amplitude follows an approximate power law. We fitted our results for $N \geq 60$ to,

$$f(N) = A N^B. \quad (50)$$

The fitting results for $T_c = 1$ GeV and $T_c = 100$ GeV are shown in [Tab. 4](#), alongside upper- and lower-bounds. A naive estimate of the peak amplitude scaling gives us $h^2 \Omega_{\text{GW}}^{\text{peak}} \propto N^{-14/3}$. The only two quantities that scale with N are the inverse duration $\tilde{\beta} \propto N^2$ and the number of degrees of freedom $g_* \propto N^2$. In combination, the peak amplitudes scales as $h^2 \Omega_{\text{GW}}^{\text{peak}} \propto \tilde{\beta}^{-2} g_*^{-1/3} \propto N^{-14/3}$. This is in good agreement with our numerical fits given in [Tab. 4](#). The numerical scaling and the naive estimate agree quite well because of cancellations between the scaling of $\tilde{\beta}$, which is not exactly N^2 , and residual N dependences in other GW parameters. It is worth highlighting that the peak amplitude scaling is mostly dominated by the inverse duration.

While we have a rather good understanding of the exponent of the N -scaling of the peak amplitude, the prefactor underlies a much larger uncertainty. This is due to the limit on supercooling discussed in [Sec. IV F](#), which we identified as the dominant uncertainty at large N . Concretely, at larger supercooling would lead to a smaller $\tilde{\beta}$ and a larger prefactor A in the peak amplitude scaling (50).

In the right panel of [Fig. 10](#), the peak frequency is plotted as a function of N using both $T_c = 1$ GeV and $T_c = 100$ GeV. The explicit dependence of f_{peak} on T_c

T_c	$\tilde{\beta}$	$h^2\Omega_{\text{GW}}^{\text{peak}}$	
	B	B	$\log_{10}(A)$
1 GeV	$2.12^{+0.08}_{-0.13}$	$-4.56^{+0.26}_{-0.34}$	$-10.74^{+0.36}_{-0.20}$
100 GeV	$2.15^{+0.07}_{-0.11}$	$-4.65^{+0.23}_{-0.29}$	$-10.57^{+0.42}_{-0.10}$

Table 4. Fit parameters for the power-law in (50) describing the large- N ($N \geq 60$) behaviour of the inverse duration and the GW power spectrum peak amplitude. The superscripts (subscripts) of the parameter values were obtained by fitting using the upper- (lower-) bounds of $\tilde{\beta}$.

explains the approximate factor of 100 difference between the two curves. The shape of the curves with N is again dominated by $\tilde{\beta}$, and the extrema of the GW peak frequency curves remain approximately at $N \simeq 12$.

In this work, we focused on the $SU(N)$ gauge group. Going beyond $SU(N)$, we expect the following two properties of the gauge group to influence how the GW spectrum changes: (I) the size of the group (the number of degrees of freedom, n_{dof} , of the adjoint representation), and (II) the centre symmetry group. The centre symmetry dictates the allowed terms in the effective Polyakov loop potential, see (15). At small N , we believe these properties may both have a noticeable impact on the strength of the signal. The centre symmetry alters the shape of the effective potential and could enter non-trivially into the interface tension and latent heat, much like n_{dof} , which goes into fixing the model parameters. This will directly affect $\tilde{\beta}$, which dominates the signal. At large N , the system is dominated by n_{dof} , and for all classical Lie groups we have $n_{\text{dof}} \propto N^2$ in this regime. Considering also that a deconfined phase minimum temperature is a feature regardless of the group, meaning there is always a limit on supercooling, we expect similar large- N scaling of the spectrum between gauge groups. However, new lattice studies are required to give a concrete answer to these questions.

B. Detectability

In Fig. 11, we plot the GW power spectrum as a function of frequency for $N = 6$ and $N = 20$ for $T_c = 100$ GeV and $T_c = 1$ GeV, respectively, alongside the power-law-integrated sensitivity curves for the LISA [105, 106], ET [107–110], CE [111, 112], DECIGO [113–116], and BBO [117–119] experiments, see [120] for a nice summary of all sensitivity curves. A better test for the detectability of a signal is given by the SNR, which is detector-dependent, but plots of the form shown in Fig. 11 are useful for understanding the wider detector landscape. We plot for $N = 6$ due to the applicability of the thin-wall approximation, and for $N = 20$ as it corresponds to the most detectable signal we found. At a critical temperature of $T_c = 100$ GeV, the GW power spectrum from the $SU(6)$ phase transition, which aligns within the bounds of ET and

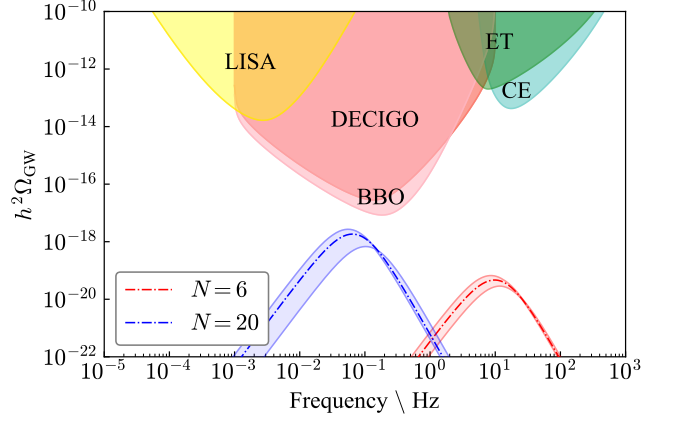


Figure 11. The stochastic GW power spectrum generated from the first-order confinement transition in $SU(N)$ pure Yang-Mills, shown for $N = 6$ (red) and $N = 20$ (blue). For $N = 6$, a critical temperature of $T_c = 100$ GeV was used, while $T_c = 1$ GeV was used for the $N = 20$ computation. The spectra are compared to the power-law-integrated sensitivity curves of the labelled GW detectors.

CE, is undetectable. That being said, the same would be true if the transition occurred at $T_c = 1$ GeV, as its peak amplitude is approximately three orders of magnitude lower than the peak of the BBO detector sensitivity. The peak amplitude of the power spectrum from the $SU(20)$ confinement phase transition is significantly greater, yet likewise remains undetectable. A critical temperature slightly above $T_c = 1$ GeV appears to be optimal for its chances of detection. In contrast with the results of [38], we have found a significant reduction in the amplitude of the GW power spectrum. This is due to both the refinements made to the model itself and the more accurate estimates of the bubble wall velocity and, in turn, the efficiency factor.

In Fig. 12 we present the SNR of the phase transition at the three most sensitive detectors we considered, namely LISA, DECIGO, and BBO, for various values of N and T_c . The left-hand plot shows the SNR as a function of N at each of these detectors, evaluated at T_c^{peak} . This is the value of the critical temperature for which the peak frequency of $h^2\Omega_{\text{GW}}(f)$ aligns exactly with the trough of the detector sensitivity curve. Therefore, this is the optimal value of T_c , and the SNRs shown are of the best-case scenario for detection. Here, we make the optimistic assumption that a signal with $\text{SNR} > 1$ is detectable. Despite this, we see that each signal predicted using the PLM is undetectable at the GW observatories. This is true even within the error bars, however, as is discussed in Sec. V C, we believe the error bars to be an underestimate for larger values of N . Around the SNR peak of $N \simeq 20$, a broader error estimate could imply a possibly detectable signal.

In the right panel of Fig. 12, we display the SNR at BBO for $N = 6$ and $N = 20$ as a function of T_c . At BBO, both signals are peaked around $T_c^{\text{peak}} = 1 - 10$ GeV.

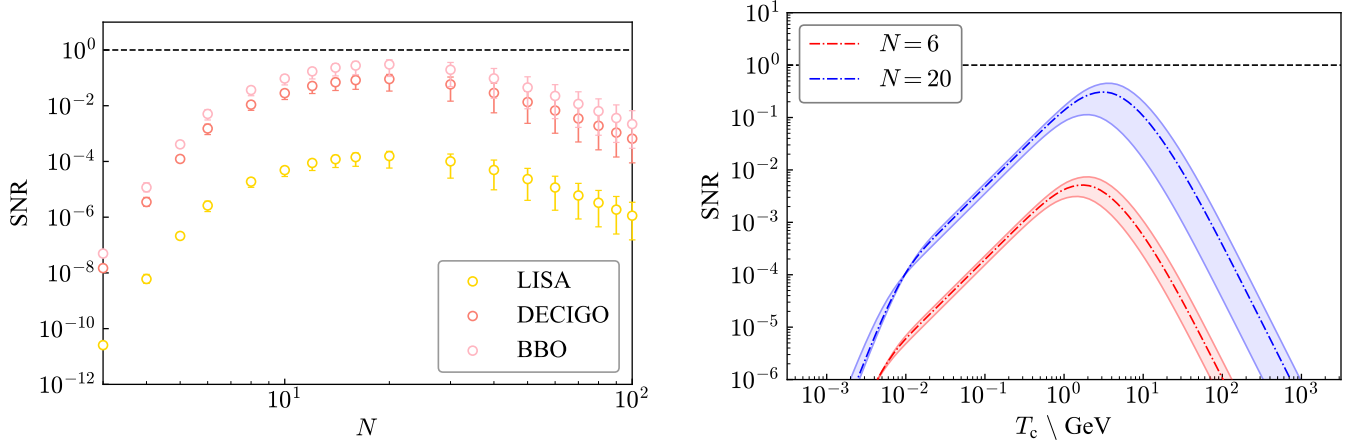


Figure 12. Signal-to-noise ratio for the confinement transition in an $SU(N)$ hidden sector. Left: as a function of N evaluated at T_c^{peak} ; the critical temperature for which the peak of the $SU(N)$ GW power spectrum and the trough of the detector sensitivity curve align. Right: as a function of T_c for $N = 6$ and $N = 20$ from the BBO experiment. The observation time is taken to be three years.

Moving away from the peak, if the critical temperature were to change by a factor of ten, we see suppression of the SNR by an order of magnitude in the best case. So, while it could be that the possible detectability of, for instance, the $N = 20$ phase transition is restored with a better error estimate, one would still require the critical temperature to be approximately equal to T_c^{peak} for hope of a detection.

Our analysis suggests that planned and future GW observatories will not probe the parameter space of a first-order confinement phase transition in an $SU(N)$ dark sector. However, while an $SU(N)$ dark sector is a natural extension of the Standard Model, it does not provide a viable single-component dark matter candidate since the corresponding parameter space of dark glueballs is largely ruled out [5, 6]. In this light, our work provides conceptual development of a more rigorous treatment of a strongly-coupled dark phase transition, and paves the way towards studying more realistic QCD-like dark sectors, including fermions [41–43, 121]. We look forward to implementing improved lattice fits through modified kinetic terms, and a consistent wall velocity in these models.

C. Discussion of Errors

In this section, we evaluate the accuracy of the error estimates given by the error bars in Figs. 10 to 12. These upper- and lower-bounds were obtained from the fitting and matching procedures described in Sec. IIIB, and correspond to the uncertainties quoted on the interface tension and latent heat from the lattice. We believe these error estimates to be sufficient where thin-wall applies, but expect them to underestimate the uncertainty at large N . There are other sources of error which are not included in these error bars that need to be illuminated.

Firstly, we comment again on the uncertainty associated with the minimum temperature at large N , this time in the context of the plots in Figs. 10 and 12, see Sec. IV F for a discussion of the GW parameters in this context. To summarise: in this work, we access large N by a rescaling of the $N = 6$ effective potential (24). This assumes that $N = 6$ is already large, and implies that the minimum temperature is a constant for $N \geq 6$, $\tau_{\text{min}}^{N=6} = \tau_{\text{min}}^{N \geq 6}$. If this assumption holds, then the presented error bars at large N are accurate. Conversely, if τ_{min}^N settles at a lower value than $\tau_{\text{min}}^{N=6}$, we would find a larger degree of supercooling and thus a larger GW signal at large N . In this respect, our results at large N of the GW spectrum peak amplitude and SNR should be taken as a lower bound, but given we expect the true minimum temperature to be only slightly lower than $\tau_{\text{min}}^{N=6}$, the resulting signals would remain weak. In summary, this implies that we might have underestimated the upper error bar at large N . Independent of the degree of supercooling at large N , the results presented in this work act as a useful guide for the expected behaviour in the GW power spectrum at large N .

The results at small N are more accurate, given the agreement with the thin-wall approximation, and we believe the error bar to be a better estimate. However, there are hidden sources of uncertainty that the error band does not take into account. To estimate the wall velocity in this work we employed the novel method presented in [52], which applies in theories where there is a large jump in the number of degrees of freedom across the phase transition. In $SU(N)$ Yang-Mills theory, where this change scales as N^2 , the large-jump assumption only strictly holds for large values of N . This introduces potentially significant uncertainty in the wall velocity at small N , which is not accounted for in the error bar. As N increases, the large-jump assumption holds more strongly and this uncertainty

drops. We also highlight that this directly impacts the uncertainty associated with the efficiency factor, which is inherently uncertain given the choice to use a constant sound speed and the fits given in (47). We expect our estimates of κ_{sw} are conservative, particularly for large N .

In the final computation of the GW power spectrum, there is one important phenomenon we have not taken into account, namely, the reheating of the plasma. The problem is nicely summarised in [122]. The general idea is the following: in a supercooled phase transition, the difference in free energy between the false and true vacua is released. This energy can manifest itself in various forms, an example of which is the kinetic energy of the plasma, which is given by κ_{sw} , and indeed it can also go into reheating the plasma. In [123], a detailed study of the impact of this reheating effect in FOPTs proceeding through subsonic deflagrations was performed. It was found that the reheating of the plasma in front of the bubble wall decreases the rate of further bubble nucleation. Notably, the effect was enhanced for greater values of $\tilde{\beta}$ and α . In the end, the suppressed bubble nucleation increased the average separation of nucleated bubbles, leading to more violent collisions. The overall effect was to increase the amplitude of the GW spectrum. We expect this to have a noticeable effect in the $SU(N)$ confinement phase transition studied here; the PLM generally exhibited very large values of $\tilde{\beta}$, which strongly suppressed the signal. We also point out the N^2 -scaling of the latent heat and relatively small degree of supercooling. Furthermore, in [124], reheating of the plasma during bubble wall collisions is identified to cause the reformation of droplets of the metastable phase, which decreases the bubble wall velocity. This effect would act to suppress the final GW signal. One therefore requires a proper treatment of this phenomenon, which was beyond the scope of this work, and we postpone it to future studies.

VI. CONCLUSIONS

We have presented a detailed computation of the gravitational wave signal generated during the confinement phase transition in $SU(N)$ pure Yang-Mills theory. Our work refines the effective Polyakov loop model developed in [38] by incorporating recent lattice results, which clarify the large- N scaling of the interface tension. Specifically, the identification of $\sigma \propto N^2$ scaling from the lattice [14] led to the introduction of a δN^2 prefactor for the kinetic term to reproduce this feature in the effective model, see Fig. 3. The parameter δ was tuned to precisely match these results, but remained of the same order for all N .

We compared the results of the phase transition inverse duration, $\tilde{\beta}$, from the Polyakov loop model to the thin-wall approximation. For small values of N , specifically $N \leq 6$, we found strong agreement, given the exact matching of the PLM to lattice data and similar predictions for the (small) degree of supercooling. At large N we

demonstrated the breakdown of the thin-wall approximation, which is attributed primarily to the presence of a minimum temperature of the deconfined phase predicted only in the effective model. The comparison between the PLM and the thin-wall approximation is shown in Fig. 6. The agreement with thin-wall at small N is a notable result of this work.

To estimate the wall velocity, we employed the novel framework [52], which assumes a large change in the number of degrees of freedom at the phase transition. Particularly in the large- N limit, this approach is applicable to the $SU(N)$ Yang-Mills theory, which has $\Delta n_{\text{dof}} \propto N^2$. We found wall velocities comparable to those obtained in [52] using the dark holographic model presented in [26]. The identification of a suitable estimate for the wall velocity is a significant improvement made compared to previous studies [34, 36–42], which generally have left it as a free parameter.

We analysed the large- N behaviour of the gravitational wave parameters and, in turn, that of the GW spectrum. In the large- N limit, we found that the nucleation temperature approached the minimum temperature of the deconfined phase. This meant quantities with no explicit N -dependence, such as the strength parameter α , and wall velocity, ξ_w , also became constant in this limit. The inverse duration exhibited $\tilde{\beta} \propto N^{2.12}$ scaling in this regime, in rough agreement with the naive N^2 estimate. This quantity was found to dominate the analysis.

For all N , we obtained rather weak gravitational wave signals, primarily due to the large suppression from $\tilde{\beta}$. The strongest signal we found was that from the $N = 20$ phase transition, which itself is undetectable at future experiments. However, due to certain assumptions made in the computations, we expect these to be conservative results. A notable result of this work was to demonstrate the suppression of the GW signal at large N .

To estimate the uncertainty on the predictions for the GW spectrum, we incorporated the error bars on the lattice results for the interface tension and latent heat in our calculation. While we expect this to be a reasonable error estimate at small N , this is an underestimate of the uncertainty for larger values of N . A number of sources of uncertainty were not quantified in the error bar, such as the reheating of the plasma, which was not considered in this work. A significant source of error at large N , which was discussed extensively, is the minimum temperature of the deconfined phase. New lattice studies are required to investigate this further.

Overall, we have provided conceptual development to accurately determine the GW spectrum of an $SU(N)$ confinement phase transition. This was achieved by improving the effective Polyakov loop model such that it accurately reproduces all lattice data, including novel surface tension results at large N . We have determined that the GW signal will not be detectable at future GW observatories, and the peak amplitude rapidly decays at large N , $h^2 \Omega_{\text{GW}}^{\text{peak}} \propto N^{-14/3}$. The weak signals are a consequence of the inherent strong coupling, which leads

to a rapidly changing effective potential. This in turn destabilises the metastable vacuum close to the critical temperature, leading to a small maximum degree of supercooling, $1 - T_{\min}/T_c \ll 1$. Despite this small supercooling, we demonstrate that the thin-wall approximation breaks down at large N . This is as a result of the disappearance of the barrier at T_{\min} . At temperatures slightly above this, where the barrier is small, the nucleated bubbles are small, and the thin-wall approximation is not applicable.

Our work paves the way for studies of dark sectors described by different symmetry groups, and more realistic QCD-like sectors containing fermions in various representations. Further lattice results for quantities such as the interface tension, latent heat, or direct information on the potential would be welcome to constrain the

corresponding effective models. In particular, QCD-like sectors close to the conformal Banks-Zaks window might offer intriguing features where the GW signal is enhanced.

Acknowledgements

We thank Mark Hindmarsh, Biagio Lucini, David Mason, Maurizio Piai, Davide Vadacchino, Jorinde van de Vis, Zhi-Wei Wang, and Fabian Zierler for discussions. This work is supported by the Science and Technology Research Council (STFC) under the Consolidated Grant ST/X000796/1, the Ernest Rutherford Fellowship ST/Z510282/1, and the STFC Studentship Grant ST/Y509620/1.

-
- [1] A. Hietanen, R. Lewis, C. Pica and F. Sannino, *Composite Goldstone Dark Matter: Experimental Predictions from the Lattice*, *JHEP* **12** (2014) 130 [[1308.4130](#)].
 - [2] Y. Bai and P. Schwaller, *Scale of dark QCD*, *Phys. Rev. D* **89** (2014) 063522 [[1306.4676](#)].
 - [3] Y. Hochberg, E. Kuflik, T. Volansky and J. G. Wacker, *Mechanism for Thermal Relic Dark Matter of Strongly Interacting Massive Particles*, *Phys. Rev. Lett.* **113** (2014) 171301 [[1402.5143](#)].
 - [4] G. D. Kribs and E. T. Neil, *Review of strongly-coupled composite dark matter models and lattice simulations*, *Int. J. Mod. Phys. A* **31** (2016) 1643004 [[1604.04627](#)].
 - [5] P. Carenza, R. Pasechnik, G. Salinas and Z.-W. Wang, *Glueball Dark Matter Revisited*, *Phys. Rev. Lett.* **129** (2022) 261302 [[2207.13716](#)].
 - [6] P. Carenza, T. Ferreira, R. Pasechnik and Z.-W. Wang, *Glueball dark matter*, *Phys. Rev. D* **108** (2023) 123027 [[2306.09510](#)].
 - [7] E. Bennett, J. Holligan, D. K. Hong, J.-W. Lee, C. J. D. Lin, B. Lucini et al., *Color dependence of tensor and scalar glueball masses in Yang-Mills theories*, *Phys. Rev. D* **102** (2020) 011501 [[2004.11063](#)].
 - [8] M. Bruno, N. Fozano, M. Panero and A. Smecca, *Thermal evolution of dark matter in the early universe from a symplectic glueball model*, [2410.17122](#).
 - [9] J. B. Kogut, H. Matsuoka, M. Stone, H. W. Wyld, S. H. Shenker, J. Shigemitsu et al., *Quark and Gluon Latent Heats at the Deconfinement Phase Transition in $SU(3)$ Gauge Theory*, *Phys. Rev. Lett.* **51** (1983) 869.
 - [10] B. Svetitsky and F. Fucito, *Latent Heat of the $SU(3)$ Gauge Theory*, *Phys. Lett. B* **131** (1983) 165.
 - [11] P. de Forcrand, B. Lucini and M. Vettorazzo, *Measuring interface tensions in 4d $SU(N)$ lattice gauge theories*, *Nucl. Phys. B Proc. Suppl.* **140** (2005) 647 [[hep-lat/0409148](#)].
 - [12] B. Lucini, M. Teper and U. Wenger, *Properties of the deconfining phase transition in $SU(N)$ gauge theories*, *JHEP* **02** (2005) 033 [[hep-lat/0502003](#)].
 - [13] M. Panero, *Thermodynamics of the QCD plasma and the large- N limit*, *Phys. Rev. Lett.* **103** (2009) 232001 [[0907.3719](#)].
 - [14] T. Rindlisbacher, K. Rummukainen and A. Salami, *Confined-deconfined interface tension and latent heat in $SU(N)$ gauge theory*, *Phys. Rev. D* **112** (2025) 114507 [[2506.15509](#)].
 - [15] E. Bennett, B. Lucini, D. Mason, M. Piai, E. Rinaldi and D. Vadacchino, *Density of states method for symplectic gauge theories at finite temperature*, *Phys. Rev. D* **111** (2025) 114511 [[2409.19426](#)].
 - [16] TELOS collaboration, *Finite-temperature Yang-Mills theories with the density of states method: towards the continuum limit*, [2509.19009](#).
 - [17] J. Braun, H. Gies and J. M. Pawłowski, *Quark Confinement from Color Confinement*, *Phys. Lett. B* **684** (2010) 262 [[0708.2413](#)].
 - [18] J. Braun, A. Eichhorn, H. Gies and J. M. Pawłowski, *On the Nature of the Phase Transition in $SU(N)$, $Sp(2)$ and $E(7)$ Yang-Mills theory*, *Eur. Phys. J. C* **70** (2010) 689 [[1007.2619](#)].
 - [19] T. K. Herbst, J. M. Pawłowski and B.-J. Schaefer, *The phase structure of the Polyakov-quark-meson model beyond mean field*, *Phys. Lett. B* **696** (2011) 58 [[1008.0081](#)].
 - [20] H. Reinhardt and J. Heffner, *The effective potential of the confinement order parameter in the Hamilton approach*, *Phys. Lett. B* **718** (2012) 672 [[1210.1742](#)].
 - [21] L. M. Haas, R. Stiele, J. Braun, J. M. Pawłowski and J. Schaffner-Bielich, *Improved Polyakov-loop potential for effective models from functional calculations*, *Phys. Rev. D* **87** (2013) 076004 [[1302.1993](#)].
 - [22] L. Fister and J. M. Pawłowski, *Confinement from Correlation Functions*, *Phys. Rev. D* **88** (2013) 045010 [[1301.4163](#)].
 - [23] P. Creminelli, A. Nicolis and R. Rattazzi, *Holography and the electroweak phase transition*, *JHEP* **03** (2002) 051 [[hep-th/0107141](#)].
 - [24] G. Nardini, M. Quiros and A. Wulzer, *A Confining Strong First-Order Electroweak Phase Transition*, *JHEP* **09** (2007) 077 [[0706.3388](#)].
 - [25] U. Gursoy, E. Kiritsis, L. Mazzanti and F. Nitti, *Holography and Thermodynamics of 5D Dilaton-gravity*, *JHEP* **05** (2009) 033 [[0812.0792](#)].
 - [26] U. Gursoy, E. Kiritsis, L. Mazzanti and F. Nitti, *Improved Holographic Yang-Mills at Finite Temperature: Comparison with Data*, *Nucl. Phys. B* **820** (2009) 148

- [0903.2859].
- [27] B. von Harling and G. Servant, *QCD-induced Electroweak Phase Transition*, *JHEP* **01** (2018) 159 [1711.11554].
- [28] P. Baratella, A. Pomarol and F. Rompineve, *The Supercooled Universe*, *JHEP* **03** (2019) 100 [1812.06996].
- [29] B. M. Dillon, B. K. El-Menoufi, S. J. Huber and J. P. Manuel, *Rapid holographic phase transition with brane-localized curvature*, *Phys. Rev. D* **98** (2018) 086005 [1708.02953].
- [30] F. Bigazzi, A. Caddeo, A. L. Cotrone and A. Paredes, *Fate of false vacua in holographic first-order phase transitions*, *JHEP* **12** (2020) 200 [2008.02579].
- [31] K. Agashe, P. Du, M. Ekhterachian, S. Kumar and R. Sundrum, *Cosmological Phase Transition of Spontaneous Confinement*, *JHEP* **05** (2020) 086 [1910.06238].
- [32] F. R. Ares, O. Henriksson, M. Hindmarsh, C. Hoyos and N. Jokela, *Effective actions and bubble nucleation from holography*, *Phys. Rev. D* **105** (2022) 066020 [2109.13784].
- [33] F. Bigazzi, A. Caddeo, A. L. Cotrone and A. Paredes, *Dark Holograms and Gravitational Waves*, *JHEP* **04** (2021) 094 [2011.08757].
- [34] F. R. Ares, M. Hindmarsh, C. Hoyos and N. Jokela, *Gravitational waves from a holographic phase transition*, *JHEP* **21** (2020) 100 [2011.12878].
- [35] F. R. Ares, O. Henriksson, M. Hindmarsh, C. Hoyos and N. Jokela, *Gravitational Waves at Strong Coupling from an Effective Action*, *Phys. Rev. Lett.* **128** (2022) 131101 [2110.14442].
- [36] E. Morgante, N. Ramberg and P. Schwaller, *Gravitational waves from dark $SU(3)$ Yang-Mills theory*, *Phys. Rev. D* **107** (2023) 036010 [2210.11821].
- [37] A. J. Helmboldt, J. Kubo and S. van der Woude, *Observational prospects for gravitational waves from hidden or dark chiral phase transitions*, *Phys. Rev. D* **100** (2019) 055025 [1904.07891].
- [38] W.-C. Huang, M. Reichert, F. Sannino and Z.-W. Wang, *Testing the dark $SU(N)$ Yang-Mills theory confined landscape: From the lattice to gravitational waves*, *Phys. Rev. D* **104** (2021) 035005 [2012.11614].
- [39] J. Halverson, C. Long, A. Maiti, B. Nelson and G. Salinas, *Gravitational waves from dark Yang-Mills sectors*, *JHEP* **05** (2021) 154 [2012.04071].
- [40] Z. Kang, J. Zhu and S. Matsuzaki, *Dark confinement-deconfinement phase transition: a roadmap from Polyakov loop models to gravitational waves*, *JHEP* **09** (2021) 060 [2101.03795].
- [41] M. Reichert, F. Sannino, Z.-W. Wang and C. Zhang, *Dark confinement and chiral phase transitions: gravitational waves vs matter representations*, *JHEP* **01** (2022) 003 [2109.11552].
- [42] R. Pasechnik, M. Reichert, F. Sannino and Z.-W. Wang, *Gravitational waves from composite dark sectors*, *JHEP* **02** (2024) 159 [2309.16755].
- [43] R. Houtz, M. Ulloa and M. West, *Gravitational Waves from Confining Dark Sectors with Self-Consistent Effective Potentials*, **2511.23467**.
- [44] R. D. Pisarski, *Quark gluon plasma as a condensate of $SU(3)$ Wilson lines*, *Phys. Rev. D* **62** (2000) 111501 [hep-ph/0006205].
- [45] R. D. Pisarski, *Effective Theory of Wilson Lines and Deconfinement*, *Phys. Rev. D* **74** (2006) 121703 [hep-ph/0608242].
- [46] M. Hindmarsh, S. J. Huber, K. Rummukainen and D. J. Weir, *Gravitational waves from the sound of a first order phase transition*, *Phys. Rev. Lett.* **112** (2014) 041301 [1304.2433].
- [47] M. Hindmarsh, S. J. Huber, K. Rummukainen and D. J. Weir, *Numerical simulations of acoustically generated gravitational waves at a first order phase transition*, *Phys. Rev. D* **92** (2015) 123009 [1504.03291].
- [48] M. Hindmarsh, S. J. Huber, K. Rummukainen and D. J. Weir, *Shape of the acoustic gravitational wave power spectrum from a first order phase transition*, *Phys. Rev. D* **96** (2017) 103520 [1704.05871].
- [49] J. T. Giblin and J. B. Mertens, *Gravitational radiation from first-order phase transitions in the presence of a fluid*, *Phys. Rev. D* **90** (2014) 023532 [1405.4005].
- [50] C. Caprini et al., *Science with the space-based interferometer eLISA. II: Gravitational waves from cosmological phase transitions*, *JCAP* **04** (2016) 001 [1512.06239].
- [51] C. Caprini et al., *Detecting gravitational waves from cosmological phase transitions with LISA: an update*, *JCAP* **03** (2020) 024 [1910.13125].
- [52] M. Sanchez-Garitaonandia and J. van de Vis, *Prediction of the bubble wall velocity for a large jump in degrees of freedom*, *Phys. Rev. D* **110** (2024) 023509 [2312.09964].
- [53] S. R. Coleman, *The Fate of the False Vacuum. 1. Semiclassical Theory*, *Phys. Rev. D* **15** (1977) 2929.
- [54] A. D. Linde, *Decay of the False Vacuum at Finite Temperature*, *Nucl. Phys. B* **216** (1983) 421.
- [55] G. M. Fuller, G. J. Mathews and C. R. Alcock, *The Quark - Hadron Phase Transition in the Early Universe: Isothermal Baryon Number Fluctuations and Primordial Nucleosynthesis*, *Phys. Rev. D* **37** (1988) 1380.
- [56] P. Agrawal, G. R. Kane, V. Loladze and M. Reig, *Supercooled confinement*, *JHEP* **10** (2025) 066 [2504.00199].
- [57] P. Agrawal, G. R. Kane, V. Loladze and J. March-Russell, *A Prediction for Maximum Supercooling in $SU(N)$ Confinement Transition*, **2508.10091**.
- [58] G. 't Hooft, *On the Phase Transition Towards Permanent Quark Confinement*, *Nucl. Phys. B* **138** (1978) 1.
- [59] G. 't Hooft, *A Property of Electric and Magnetic Flux in Nonabelian Gauge Theories*, *Nucl. Phys. B* **153** (1979) 141.
- [60] B. Svetitsky and L. G. Yaffe, *Critical Behavior at Finite Temperature Confinement Transitions*, *Nucl. Phys. B* **210** (1982) 423.
- [61] C. Ratti, M. A. Thaler and W. Weise, *Phases of QCD: Lattice thermodynamics and a field theoretical model*, *Phys. Rev. D* **73** (2006) 014019 [hep-ph/0506234].
- [62] WHOT-QCD collaboration, *Phase structure of finite temperature QCD in the heavy quark region*, *Phys. Rev. D* **84** (2011) 054502 [1106.0974].
- [63] G. Aarts et al., *Phase Transitions in Particle Physics: Results and Perspectives from Lattice Quantum Chromo-Dynamics*, *Prog. Part. Nucl. Phys.* **133** (2023) 104070 [2301.04382].
- [64] F. Sannino, *Higher representations: Confinement and large N* , *Phys. Rev. D* **72** (2005) 125006 [hep-th/0507251].

- [65] J. Polonyi and K. Szlachanyi, *Phase Transition from Strong Coupling Expansion*, *Phys. Lett. B* **110** (1982) 395.
- [66] M. Gross and J. F. Wheeler, *On The Order of the $SU(N)$ Deconfinement Phase Transition*, *Nucl. Phys. B* **240** (1984) 253.
- [67] M. Ogilvie, *An Effective Spin Model for Finite Temperature QCD*, *Phys. Rev. Lett.* **52** (1984) 1369.
- [68] H. Matsuoka, *Deconfinement Transition and the $Z(N)$ Clock Model*, *Phys. Lett. B* **140** (1984) 233.
- [69] F. Green and F. Karsch, *The $SU(4)$ Deconfining Transition at Strong Coupling: A Monte Carlo Study*, *Phys. Rev. D* **29** (1984) 2986.
- [70] K. Fukushima and V. Skokov, *Polyakov loop modeling for hot QCD*, *Prog. Part. Nucl. Phys.* **96** (2017) 154 [1705.00718].
- [71] L. Giusti, M. Hirasawa, M. Pepe and L. Virzi, *A precise study of the thermodynamic properties of the $SU(3)$ Yang-Mills theory across the deconfinement transition*, *Phys. Lett. B* **868** (2025) 139775 [2501.10284].
- [72] A. Kosowsky, M. S. Turner and R. Watkins, *Gravitational waves from first order cosmological phase transitions*, *Phys. Rev. Lett.* **69** (1992) 2026.
- [73] A. Kosowsky, M. S. Turner and R. Watkins, *Gravitational radiation from colliding vacuum bubbles*, *Phys. Rev. D* **45** (1992) 4514.
- [74] A. Kosowsky and M. S. Turner, *Gravitational radiation from colliding vacuum bubbles: envelope approximation to many bubble collisions*, *Phys. Rev. D* **47** (1993) 4372 [astro-ph/9211004].
- [75] M. Kamionkowski, A. Kosowsky and M. S. Turner, *Gravitational radiation from first order phase transitions*, *Phys. Rev. D* **49** (1994) 2837 [astro-ph/9310044].
- [76] C. Caprini, R. Durrer and G. Servant, *Gravitational wave generation from bubble collisions in first-order phase transitions: An analytic approach*, *Phys. Rev. D* **77** (2008) 124015 [0711.2593].
- [77] S. J. Huber and T. Konstandin, *Gravitational Wave Production by Collisions: More Bubbles*, *JCAP* **09** (2008) 022 [0806.1828].
- [78] D. J. Weir, *Revisiting the envelope approximation: gravitational waves from bubble collisions*, *Phys. Rev. D* **93** (2016) 124037 [1604.08429].
- [79] R. Jinno and M. Takimoto, *Gravitational waves from bubble collisions: An analytic derivation*, *Phys. Rev. D* **95** (2017) 024009 [1605.01403].
- [80] M. Hindmarsh, *Sound shell model for acoustic gravitational wave production at a first-order phase transition in the early Universe*, *Phys. Rev. Lett.* **120** (2018) 071301 [1608.04735].
- [81] J. Ellis, M. Lewicki and J. M. No, *Gravitational waves from first-order cosmological phase transitions: lifetime of the sound wave source*, *JCAP* **07** (2020) 050 [2003.07360].
- [82] C. Caprini, R. Durrer and G. Servant, *The stochastic gravitational wave background from turbulence and magnetic fields generated by a first-order phase transition*, *JCAP* **12** (2009) 024 [0909.0622].
- [83] A. Kosowsky, A. Mack and T. Kahniashvili, *Gravitational radiation from cosmological turbulence*, *Phys. Rev. D* **66** (2002) 024030 [astro-ph/0111483].
- [84] A. D. Dolgov, D. Grasso and A. Nicolis, *Relic backgrounds of gravitational waves from cosmic turbulence*, *Phys. Rev. D* **66** (2002) 103505 [astro-ph/0206461].
- [85] A. Nicolis, *Relic gravitational waves from colliding bubbles and cosmic turbulence*, *Class. Quant. Grav.* **21** (2004) L27 [gr-qc/0303084].
- [86] C. Caprini and R. Durrer, *Gravitational waves from stochastic relativistic sources: Primordial turbulence and magnetic fields*, *Phys. Rev. D* **74** (2006) 063521 [astro-ph/0603476].
- [87] G. Gogoberidze, T. Kahniashvili and A. Kosowsky, *The Spectrum of Gravitational Radiation from Primordial Turbulence*, *Phys. Rev. D* **76** (2007) 083002 [0705.1733].
- [88] T. Kahniashvili, L. Campanelli, G. Gogoberidze, Y. Maravin and B. Ratra, *Gravitational Radiation from Primordial Helical Inverse Cascade MHD Turbulence*, *Phys. Rev. D* **78** (2008) 123006 [0809.1899].
- [89] T. Kahniashvili, L. Kisslinger and T. Stevens, *Gravitational Radiation Generated by Magnetic Fields in Cosmological Phase Transitions*, *Phys. Rev. D* **81** (2010) 023004 [0905.0643].
- [90] L. Kisslinger and T. Kahniashvili, *Polarized Gravitational Waves from Cosmological Phase Transitions*, *Phys. Rev. D* **92** (2015) 043006 [1505.03680].
- [91] M. B. Hindmarsh, M. Lüben, J. Lumma and M. Pauly, *Phase transitions in the early universe*, *SciPost Phys. Lect. Notes* **24** (2021) 1 [2008.09136].
- [92] M. Breitbach, J. Kopp, E. Madge, T. Opferkuch and P. Schwaller, *Dark, Cold, and Noisy: Constraining Secluded Hidden Sectors with Gravitational Waves*, *JCAP* **07** (2019) 007 [1811.11175].
- [93] M. Fairbairn, E. Hardy and A. Wickens, *Hearing without seeing: gravitational waves from hot and cold hidden sectors*, *JHEP* **07** (2019) 044 [1901.11038].
- [94] P. Archer-Smith, D. Linthorne and D. Stolarski, *Gravitational Wave Signals from Multiple Hidden Sectors*, *Phys. Rev. D* **101** (2020) 095016 [1910.02083].
- [95] A. H. Guth and S. H. H. Tye, *Phase Transitions and Magnetic Monopole Production in the Very Early Universe*, *Phys. Rev. Lett.* **44** (1980) 631.
- [96] A. H. Guth and E. J. Weinberg, *Cosmological Consequences of a First Order Phase Transition in the $SU(5)$ Grand Unified Model*, *Phys. Rev. D* **23** (1981) 876.
- [97] Y. Bea, J. Casallerrey-Solana, T. Giannakopoulos, D. Mateos, M. Sanchez-Garitaonandia and M. Zilhão, *Bubble wall velocity from holography*, *Phys. Rev. D* **104** (2021) L121903 [2104.05708].
- [98] F. Bigazzi, A. Caddeo, T. Canneti and A. L. Cotrone, *Bubble wall velocity at strong coupling*, *JHEP* **08** (2021) 090 [2104.12817].
- [99] Y. Bea, J. Casallerrey-Solana, T. Giannakopoulos, A. Jansen, D. Mateos, M. Sanchez-Garitaonandia et al., *Holographic bubbles with Jecco: expanding, collapsing and critical*, *JHEP* **09** (2022) 008 [2202.10503].
- [100] R. A. Janik, M. Jarvinen, H. Soltanpanahi and J. Sonnenschein, *Perfect Fluid Hydrodynamic Picture of Domain Wall Velocities at Strong Coupling*, *Phys. Rev. Lett.* **129** (2022) 081601 [2205.06274].
- [101] J. R. Espinosa, T. Konstandin, J. M. No and G. Servant, *Energy Budget of Cosmological First-order Phase Transitions*, *JCAP* **06** (2010) 028 [1004.4187].
- [102] W.-Y. Ai, B. Laurent and J. van de Vis, *Bounds on the*

- bubble wall velocity, *JHEP* **02** (2025) 119 [[2411.13641](#)].
- [103] H.-K. Guo, K. Sinha, D. Vagie and G. White, *Phase Transitions in an Expanding Universe: Stochastic Gravitational Waves in Standard and Non-Standard Histories*, *JCAP* **01** (2021) 001 [[2007.08537](#)].
 - [104] C. Caprini, R. Jinno, T. Konstandin, A. Roper Pol, H. Rubira and I. Stomberg, *Gravitational waves from first-order phase transitions: from weak to strong*, *JHEP* **07** (2025) 217 [[2409.03651](#)].
 - [105] LISA collaboration, *Laser Interferometer Space Antenna*, [1702.00786](#).
 - [106] J. Baker et al., *The Laser Interferometer Space Antenna: Unveiling the Millihertz Gravitational Wave Sky*, [1907.06482](#).
 - [107] M. Punturo et al., *The Einstein Telescope: A third-generation gravitational wave observatory*, *Class. Quant. Grav.* **27** (2010) 194002.
 - [108] S. Hild et al., *Sensitivity Studies for Third-Generation Gravitational Wave Observatories*, *Class. Quant. Grav.* **28** (2011) 094013 [[1012.0908](#)].
 - [109] B. Sathyaprakash et al., *Scientific Objectives of Einstein Telescope*, *Class. Quant. Grav.* **29** (2012) 124013 [[1206.0331](#)].
 - [110] ET collaboration, *Science Case for the Einstein Telescope*, *JCAP* **03** (2020) 050 [[1912.02622](#)].
 - [111] LIGO SCIENTIFIC collaboration, *Exploring the Sensitivity of Next Generation Gravitational Wave Detectors*, *Class. Quant. Grav.* **34** (2017) 044001 [[1607.08697](#)].
 - [112] D. Reitze et al., *Cosmic Explorer: The U.S. Contribution to Gravitational-Wave Astronomy beyond LIGO*, *Bull. Am. Astron. Soc.* **51** (2019) 035 [[1907.04833](#)].
 - [113] S. Isoyama, H. Nakano and T. Nakamura, *Multiband Gravitational-Wave Astronomy: Observing binary inspirals with a decihertz detector*, *B-DECIGO*, *PTEP* **2018** (2018) 073E01 [[1802.06977](#)].
 - [114] K. Yagi and N. Seto, *Detector configuration of DECIGO/BBO and identification of cosmological neutron-star binaries*, *Phys. Rev. D* **83** (2011) 044011 [[1101.3940](#)].
 - [115] S. Kawamura et al., *The Japanese space gravitational wave antenna DECIGO*, *Class. Quant. Grav.* **23** (2006) S125.
 - [116] N. Seto, S. Kawamura and T. Nakamura, *Possibility of direct measurement of the acceleration of the universe using 0.1-Hz band laser interferometer gravitational wave antenna in space*, *Phys. Rev. Lett.* **87** (2001) 221103 [[astro-ph/0108011](#)].
 - [117] J. Crowder and N. J. Cornish, *Beyond LISA: Exploring future gravitational wave missions*, *Phys. Rev. D* **72** (2005) 083005 [[gr-qc/0506015](#)].
 - [118] V. Corbin and N. J. Cornish, *Detecting the cosmic gravitational wave background with the big bang observer*, *Class. Quant. Grav.* **23** (2006) 2435 [[gr-qc/0512039](#)].
 - [119] G. M. Harry, P. Fritschel, D. A. Shaddock, W. Folkner and E. S. Phinney, *Laser interferometry for the big bang observer*, *Class. Quant. Grav.* **23** (2006) 4887.
 - [120] K. Schmitz, *New Sensitivity Curves for Gravitational-Wave Signals from Cosmological Phase Transitions*, *JHEP* **01** (2021) 097 [[2002.04615](#)].
 - [121] P. Schwaller, *Gravitational Waves from a Dark Phase Transition*, *Phys. Rev. Lett.* **115** (2015) 181101 [[1504.07263](#)].
 - [122] P. Athron, C. Balázs, A. Fowlie, L. Morris and L. Wu, *Cosmological phase transitions: From perturbative particle physics to gravitational waves*, *Prog. Part. Nucl. Phys.* **135** (2024) 104094 [[2305.02357](#)].
 - [123] M. A. Ajmi and M. Hindmarsh, *Thermal suppression of bubble nucleation at first-order phase transitions in the early Universe*, *Phys. Rev. D* **106** (2022) 023505 [[2205.04097](#)].
 - [124] D. Cutting, M. Hindmarsh and D. J. Weir, *Vorticity, kinetic energy, and suppressed gravitational wave production in strong first order phase transitions*, *Phys. Rev. Lett.* **125** (2020) 021302 [[1906.00480](#)].